

Impacts of Atmospheric Internal Variations on the Variability of Sea Surface Temperature based on the Hydra-SINTEX Model

Yi Zhang¹, Jiye Wu¹, Yongjun Zheng¹, and Jing-Jia Luo¹

¹Institute for Climate and Application Research (ICAR)/CIC-FEMD/KLME, Nanjing University
of Information Science & Technology (NUIST), Nanjing, China

Corresponding author: Jing-Jia Luo (jjluo@nuist.edu.cn; jingjia_luo@hotmail.com)

Key points:

- A developed interactive ensemble model is to investigate the impacts of atmospheric internal variations (AIVs) on climate variabilities
- The results suggest that the AIVs largely impacts sea surface temperature variability but with distinct regional features
- Without the AIVs, variabilities of the sea surface temperature in the tropics and extra-tropics are much reduced

Abstract

Ocean–atmosphere interactions largely control the variabilities of the climate system on Earth. However, how much atmospheric internal signals contribute to climate variabilities remains uncertain over many parts of the globe. Here, we develop an interactive ensemble coupled model (called Hydra-SINTEX) to investigate the influences of atmospheric internal variations (AIVs) on the mean-states and variability of the climate system. The results show that, while climatological mean-states are little affected, the AIVs can largely influence climate variabilities over the globe. We pay particular attention to two regions, i.e., the tropical eastern Indian Ocean, which is the key area of the Indian Ocean Dipole (IOD), and the subtropical North Pacific. We found that sea surface temperature (SST) variabilities in these two regions are much reduced without the AIVs but with distinct mechanisms. Without the AIVs, the intensity of the IOD is largely reduced in association with weakened air–sea coupling in the tropics. This indicates the importance of atmospheric noise forcing on the development of the IOD. In contrast, the reduction of SST variability in the subtropical North Pacific is caused by the absence of the AIVs that are generated by both mid-latitude atmospheric processes and weakened remote influence of the tropical SST in accordance with the reduced SST signals there.

Plain Language Summary

Ocean–atmosphere interactions are pivotal in shaping Earth’s climate system. However, how much atmospheric internal variations (AIVs) contribute to climate variabilities remains uncertain in many places over the globe. Here, we have devised an interactive ensemble coupled model (called Hydra-SINTEX), allowing us to explore the impacts of the AIVs on the mean-states and variabilities of the climate system. The results reveal that, while climatological mean-states remain little affected, the AIVs significantly influence global climate variabilities. We focus on two specific regions: the tropical eastern Indian Ocean, a critical area for the Indian Ocean Dipole (IOD), and the subtropical North Pacific. We have observed that SST variabilities in these regions are notably reduced in the absence of the AIVs through distinct mechanisms. In the case of the IOD, the absence of the AIVs leads to a considerable decrease in its intensity. This underscores the significance of atmospheric noise forcing in influencing the development of the IOD. Conversely, the reduction of SST variability in the subtropical North Pacific can be attributed to the absence of

the AIVs generated by mid-latitude atmospheric processes and the diminished influence of tropical SST signals.

1 Introduction

Among variabilities of geophysical variables that need to be quantified, sea surface temperature (SST) variability, due to its significant contributions, plays a pivotal role in the predictability of climate variations (Straus et al., 2003). For instance, El Niño–Southern Oscillation (ENSO) and Indian Ocean Dipole (IOD; Saji et al., 1999) serve as two leading sources of seasonal–interannual predictability of global climate.

The SST variability is demonstrated to be jointly contributed by oceanic processes (e.g., Capotondi et al., 2023), ocean–atmosphere coupled feedbacks (e.g., Latif & Barnett, 1994), and atmospheric internal variations (AIVs) (e.g., Capotondi et al., 2023; Hasselmann, 1976; Shukla, 1981). Meanwhile, mechanisms dictating SST variability exhibit distinctions between tropics and mid-latitudes. The Bjerknes positive feedback (Bjerknes, 1969) plays a significant role in the emergence of tropical climate modes like ENSO and IOD. On the contrary, SST variability in mid-latitudes involves numerous processes. For example, sources of SST variability in the North Pacific include local atmospheric stochastic forcing (Hasselmann, 1976), air–sea coupled feedback (Latif & Barnett, 1994), and remote influences from other parts of the world, such as tropical Pacific (Alexander et al., 2002) and the North Atlantic (Deser et al., 2004). Note that oceanic processes and ocean–atmosphere coupled feedbacks are slow-varying and hence largely predictable, while the AIVs are characterized by high frequency and hardly predicted (e.g., Deser et al., 2014). Hence, it is imperative to quantify the extent to which the AIVs can affect overall SST variability to gain deeper insights into the predictability of various climate modes.

Traditionally, the AIVs and forced components by SST variations have typically been recognized and investigated through an ensemble of Atmospheric Model Intercomparison Project (AMIP) simulations (Hannachi, 2001; Hoerling et al., 1997; Shukla et al., 2000; Straus & Shukla, 2000; Zwiers, 1996). The forced variations from prescribed SST in the AMIP are established through the ensemble mean, while internal variations are calculated by subtracting the ensemble mean from each individual ensemble member. Nevertheless, this approach could encounter issues with energetic inconsistency in terms of atmospheric forcings, specifically when SSTs fail to respond to atmospheric fluxes (Kirtman et al., 2009; Van den Dool et al., 2006; Wu & Kirtman, 2005). Meanwhile, the method confines the analysis to atmospheric variables and is solely suitable for distinguishing the SST-forced signal from climate-related noise (i.e., AIVs). Besides, it lacks the inherent capability to separate SST variability into signal and noise components without the application of specific temporal and spatial filters (Yeh & Kirtman, 2006).

To overcome the aforementioned limitations, Kirtman and Shukla (2002) proposed an interactive ensemble (IE) technique to mitigate the potential impact of the AIVs (Wu & Kirtman, 2003, 2006) and devised an interactive ensemble coupled model leveraging the standard coupling (SC) model as its foundation (Figure 1a, b). The elimination of the AIVs in the IE is by transferring ensemble mean forcings of multiple atmosphere components to a single oceanic component at each coupling step. At the same time, only a single oceanic component provides sea ice, surface currents, and SST conditions to each atmosphere component. In the IE, the effects of AIVs on the ENSO were investigated by Kirtman and Shukla (2002) and Yeh and Kirtman (2009), and they discovered that the IE model is quite capable of fairly accurate simulations of ENSO. Besides, ENSO variance is roughly 25% less in the IE than in the SC model. ENSO oscillations in the IE

are primarily characterized by a biennial cycle, whereas the SC exhibits a wider spectral peak spanning between 2 and 4 years.

However, another important climate mode—IOD in the tropical Indian Ocean—also exists, but without sufficient examination in the IE, which has been proven to be largely influenced by the AIVs (Ng et al., 2018). Furthermore, earlier studies have indicated that mid-latitude atmospheric internal processes are pivotal in the variability of the North Pacific SST, with secondary effects of remote forcing from tropical SST (Yeh et al., 2007; Yeh & Kirtman, 2004). However, the schemes for isolating mid-latitude atmospheric processes and remote influence from tropical SST are artificial assumptions with a lack of scientific evidence. A more comprehensive analysis is needed to assess the extent to which mid-latitude atmospheric processes and remote influence from tropical SST can affect the variability of the North Pacific SST. Therefore, we perform two experiments in our study, IE (i.e., Hydra-SINTEX) and SC (i.e., SINTEX-F), and analyze differences between them to examine how the AIVs impact SST variability.

The following context is organized as below. A description of the experimental design, observational datasets, and methods is given in Section 2. In Section 3, we quantify the AIVs and their relative importance to climate variabilities. Section 4 provides the mean-states and variability of SST in the IE and SC. In Section 5, we focus on the AIVs' effects on two specific regions: the tropical eastern Indian Ocean and the subtropical North Pacific Ocean. A summary and discussions are provided in Section 6.

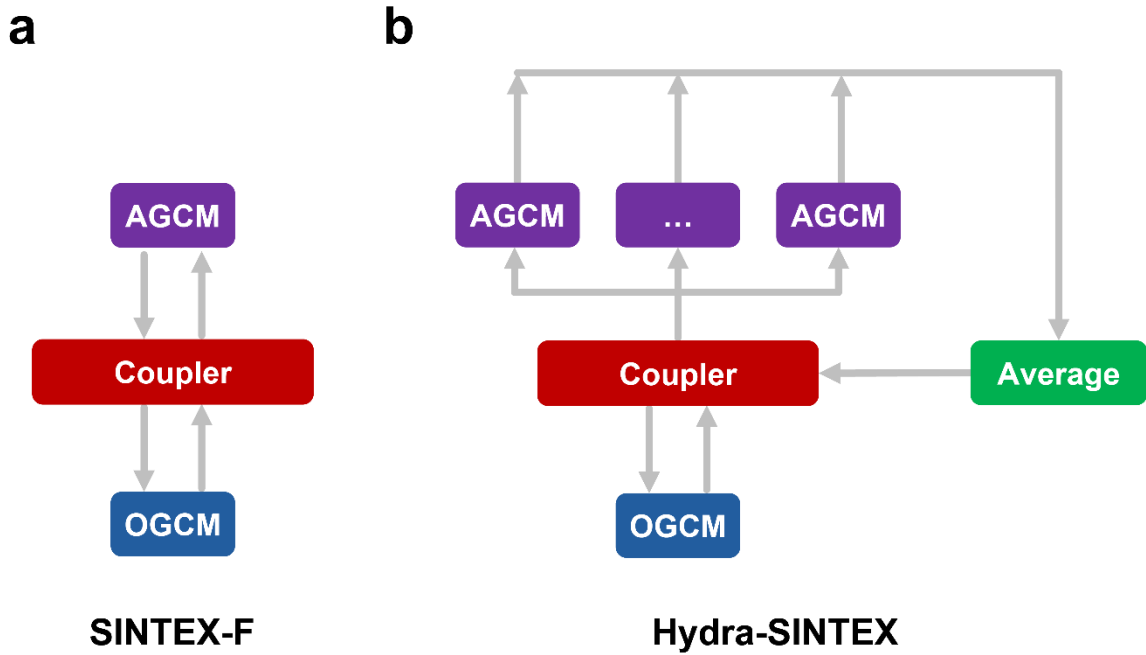


Figure 1. (a) The standard coupled model (i.e., SINTeX-F) and (b) interactive ensemble coupled model scheme (i.e., Hydra-SINTeX). The grey arrows indicate the flow direction of variables exchanged between the atmosphere and ocean models at each coupling step.

2 Data and Methods

2.1 Experimental Design and Observational Datasets

The SINTeX-F (Figure 1a) is a standard coupled ocean–atmosphere model jointly developed through collaboration between the European Union and Japan (Gualdi et al., 2003; Luo et al., 2003; Luo, Masson, Roeckner, et al., 2005). The atmospheric component (AGCM) is constructed by the fourth generation of ECHAM (Roeckner et al., 1996). It boasts a horizontal resolution of T106 ($1.1^\circ \times 1.1^\circ$) and incorporates 19 hybrid sigma-pressure levels in the vertical dimension. The oceanic component (OGCM) is implemented by Océan Parallélisé (OPA) version 8.2 (Madec et al., 1998). It is globally configured with ORCA2 settings (Madec & Imbard, 1996).

Within this configuration, the OGCM maintains an average horizontal resolution of $2^{\circ} \times 2^{\circ}$ across 31 vertical levels, with layer thickness ranging from 10 meters to 500 meters. Additionally, there is an improved meridional resolution of $0.5^{\circ} \times 0.5^{\circ}$ in the vicinity of the equator. The OASIS 2.4 coupler (Valcke et al., 2000) facilitates couplings for atmospheric and oceanic components at two-hour intervals.

On the basis of the SINTEX-F, we have created an interactive ensemble variant known as Hydra-SINTEX (Figure 1b), featuring nine identical atmospheric components coupled with a single oceanic component. The only difference across identical atmosphere components is the initial fields. They are generated by the coupled SST-nudging initialization schemes that are utilized in the Nanjing University of Information Science and Technology Climate Forecast System 1.0 (NUIST-CFS 1.0), developed based on SINTEX-F (He et al., 2023; He et al., 2020; Luo et al., 2008). Due to the high sensitivity of the atmosphere to initial fields, atmospheric components can exhibit divergent evolutions from one another.

We conducted two experiments spanning a 200-year length for the SINTEX-F and Hydra-SINTEX (Table 1). The full coupling wind stress scheme (Luo, Masson, Behera, et al., 2005; Pacanowski, 1987) is employed in all experiments. For the initial 20-year spin-up period, all experiments are integrated with transient carbon dioxide observational data from the Global Monitoring Laboratory (GML) of the National Oceanic and Atmospheric Administration (NOAA) during 2000–2020 and then with a constant value in 2020 during the remaining 180-year integration period for a free coupled run. In subsequent analysis, only the last 180-year integration is adopted. The SST observational data is sourced from the Optimum Interpolation Sea Surface Temperature (OISST) data (Huang et al., 2021), while the 500-hPa geopotential height data is

obtained from the ERA5 reanalysis (Hersbach et al., 2020). The observational datasets encompass the timeframe spanning from January 1982 to December 2021.

Table 1. The experimental design.

Experiment	Analysis Period	Members	Forcing
Hydra-SINTEX	180 years	9 AGCMs + 1 OGCM	Fixed external
SINTEX-F		1 AGCM + 1 OGCM	forcing

2.2 Signal, Noise, and Signal-to-noise Ratio

In the Hydra-SINTEX, all nine atmospheric components are driven by identical forcing from ocean surface currents and SST that are updated at each coupling step. Therefore, climate noise can be estimated with the ensemble spread, originating from atmospheric internally-induced variations (i.e., AIVs) and remaining independent of externally-generated signal (i.e., the ensemble mean; see Hu et al., 2021; Kumar & Hoerling, 2000). Note that, due to the limited computation resource, we can only conduct the nine-member experiment currently, and we use all the nine members to estimate the signal and AIVs.

The variable of the m -th member in the n -th month is marked by $x_{m,n}$. The overall mean is given by $\bar{x} = \frac{1}{NM} \sum_n^N \sum_m^M x_{m,n}$, and the ensemble mean is $\langle x_n \rangle = \frac{1}{M} \sum_m^M x_{m,n}$. With these definitions, we can characterize the standard deviation of signal (standard deviation of ensemble mean) and standard deviation of noise (ensemble spread) as follows:

$$\sigma_{\text{signal}} = \sqrt{\frac{1}{N} \sum_n^N (\langle x_n \rangle - \bar{x})^2}, \quad (1)$$

$$\sigma_{\text{noise}} = \sqrt{\frac{1}{NM} \sum_n^N \sum_m^M (x_{m,n} - \langle x_n \rangle)^2}. \quad (2)$$

We assume that the signal is independent of the noise, and thus, the total variability can be expressed as the combination of the signal and noise. We use the signal-to-noise ratio (SNR, i.e., $\sigma_{\text{signal}}/\sigma_{\text{noise}}$) to describe the relative importance of the signal and noise. In the case when SNR is greater than 1, the oceanic forcing plays a major role in climate variations, whereas SNR less than 1 means that the AIVs play a dominant role (Kumar & Hoerling, 2000).

2.3 Reduction Rate

We define the reduction rate to measure the AIVs' influence in the ocean-atmosphere coupled system as follows:

$$1 - \frac{\sigma_{\text{Hydra-SINTEX}}}{\sigma_{\text{SINTEX-F}}}, \quad (3)$$

where $\sigma_{\text{Hydra-SINTEX}}$ represents the standard deviations of a variable in the Hydra-SINTEX, and $\sigma_{\text{SINTEX-F}}$ represents the standard deviations of the counterpart in the SINTEX-F. The reduction rate represents the relative difference in the standard deviations of selected variables between the SINTEX-F and Hydra-SINTEX.

2.4 Levene's Test

Levene's test (Brown & Forsythe, 1974; Levene, 1960) is employed to compare variances of different groups to ascertain whether these groups possess the same variances in the overall population. The null hypothesis posits that variances across all groups are equal, while the alternative hypothesis suggests that at least one group exhibits a different variance from the others. One notable strength of Levene's test lies in its robustness against non-normal distribution and

relative sensitivity to small and moderate-sized samples, rendering it versatile and applicable in practical studies (Erjavec, 2011).

2.5 Skewness and Shapiro–Wilk Test

The k th statistical moment about the mean can be expressed as:

$$m_k = \sum_{i=1}^N \frac{(x_i - \bar{X})^k}{N}, \quad (4)$$

where x_i is the i th sample, \bar{X} is the samples mean, and N is the number of samples.

The skewness serves as a metric to quantify the asymmetry of a distribution and is defined as (Hong, Li, Linho, et al., 2008; White, 1980):

$$\text{skewness} = \frac{m_3}{(m_2)^{3/2}}. \quad (5)$$

Specifically, a skewness value of 0 denotes a sample distribution conforming to the characteristics of a normal distribution.

The Shapiro–Wilk test (Shapiro & Wilk, 1965) is a hypothesis test designed to assess the normality of a given data. This test examines a sample from the perspective of a null hypothesis, which posits that the sample follows a normal distribution. A high p-value suggests that the sample adheres to a normal distribution, while a low p-value suggests non-normality.

2.6 Niño3.4 Index and PNA Index

The Niño3.4 index is a widely employed metric for assessing ENSO evolution (Bamston et al., 1997), while the PNA index is calculated as the second principal component of the rotated

empirical orthogonal functions (REOFs) of 500-hPa monthly-mean anomalies of geopotential height across the Northern Hemisphere (20°N to 85°N) (Barnston & Livezey, 1987). The original PNA index definition (Wallace & Gutzler, 1981) entails a linear combination of the normalized 500-hPa height anomalies at the four central pattern locations, while the REOFs approach yields more robust results (Rodionov & Assel, 2001) based on the entire field. Note that both types of PNA indices produce similar results (Table S1 in Supporting Information).

2.7 The Mixed-layer Heat Budget Analysis

To pinpoint the potential causes of SST variability, we conduct an ocean mixed-layer heat budget analysis. The equation (Li et al., 2002) is formulated as follows:

$$\begin{aligned} \frac{\partial T'}{\partial t} = & \left(-\bar{u} \frac{\partial T'}{\partial x} - u' \frac{\partial \bar{T}}{\partial x} - u' \frac{\partial T'}{\partial x} \right) + \left(-\bar{v} \frac{\partial T'}{\partial y} - v' \frac{\partial \bar{T}}{\partial y} - v' \frac{\partial T'}{\partial y} \right) \\ & + \left(-\bar{w} \frac{\partial T'}{\partial z} - w' \frac{\partial \bar{T}}{\partial z} - w' \frac{\partial T'}{\partial z} \right) + \frac{Q'_{\text{net}}}{\rho c_p H} + R \end{aligned} \quad (6)$$

where T, ρ_0, H , and c_p denote the mixed-layer temperature (MLT), mean seawater density, mixed-layer depth (MLD, time-varying variable defined by 0.01 kg·m⁻³ density increase from surface), and specific heat capacity of seawater, respectively. $\frac{\partial T'}{\partial t}$ donates MLT tendency, u and v denote horizontal components of velocity, and w denotes vertical components of velocity. The prime terms represent the anomalies of variables, and the bar terms represent the mean-states of variables. The term $-\bar{u} \frac{\partial T'}{\partial x} - u' \frac{\partial \bar{T}}{\partial x}$ is the summation of linear U advection term, and the term $-u' \frac{\partial T'}{\partial x}$ represents nonlinear U advection term. Similar terms are defined for V and W components.

$\frac{Q'_{\text{net}}}{\rho c_p H}$ represents surface heat fluxes, and R represents residual error. Here, upward surface heat fluxes manifest positively.

3 Evaluation of AIVs for Geopotential Height

As mentioned above, the AIVs can be estimated with the ensemble spread based on the Hydra-SINTEX (Figure S1 in Supporting Information). The results display strong internal variabilities of geopotential height at all pressure levels in mid-high latitudes with a large spatial inhomogeneity but generally uniformly low internal variabilities in tropics. The strongest internal variability appears in the stratosphere over the Arctic region, with the magnitude being 7 times that in the equatorial zone (Figure S1e).

Correspondingly, the SNR of geopotential height is generally high in tropical regions but low in middle and high latitudes with distinctive spatial distribution among different pressure levels (Figure 2). For instance, the regions with high SNR ($\text{SNR} > 0.5$) at low troposphere are mainly confined in the Indo-Pacific Warm Pool, Maritime Continent, and equatorial eastern Pacific. From the middle troposphere to the upper troposphere, the SNR in the tropics exhibits a pronounced increase, implying a diminishing AIVs' influence on tropical atmospheric circulation. In addition, a band of high SNR emerges, encompassing the entire tropical region (Figure 2c, d). There is a sharp meridional gradient of the SNR along the southern (20° – 30° S) and northern (20° – 30° N) boundaries of the tropical band (Figure 2e). The north-south scope of the high SNR band approximately aligns with the Hadley cell (Moon & Ha, 2020). Interestingly, the zonal distribution of the tropical high SNR band is non-uniform, characterized by two maximum centers situated over the Indian Ocean and the eastern equatorial Pacific, respectively. The patterns resemble a petal-like structure seen in the Matsuno-Gill model (Garfinkel et al., 2023; Gill, 1980; Matsuno,

1966), implying the potential importance of adiabatic heating in the tropical upper troposphere. In addition, the tropical high SNR band approximately corresponds to major tropical convection zones (Argüeso et al., 2020; Izumo et al., 2020). One plausible explanation is that deep atmospheric convection depends more on the SST forcing rather than on the AIVs. The above results suggest a relatively weak influence of the AIVs on the tropical mid-upper troposphere.

After reaching the peak at the tropopause (around 70hPa; Fueglistaler et al., 2009), the SNR gradually diminishes in the stratosphere (Figure 2e), indicating an enhancement of AIVs' influence on the stratosphere, consistent with the increased AIVs in the troposphere (recall Figure S1e in Supporting Information). However, the tropical stratosphere SNR still remains significantly higher compared to those in middle and high latitudes, indicating the lower influence of the AIVs in the tropical stratosphere.

The SNR in mid-latitudes is generally low and displays a gradual increase from the surface to the upper atmosphere (Figure 2e). This indicates a strong influence of the AIVs in the mid-latitude atmosphere, with the lower troposphere exhibiting a greater influence of the AIVs compared to the upper atmosphere.

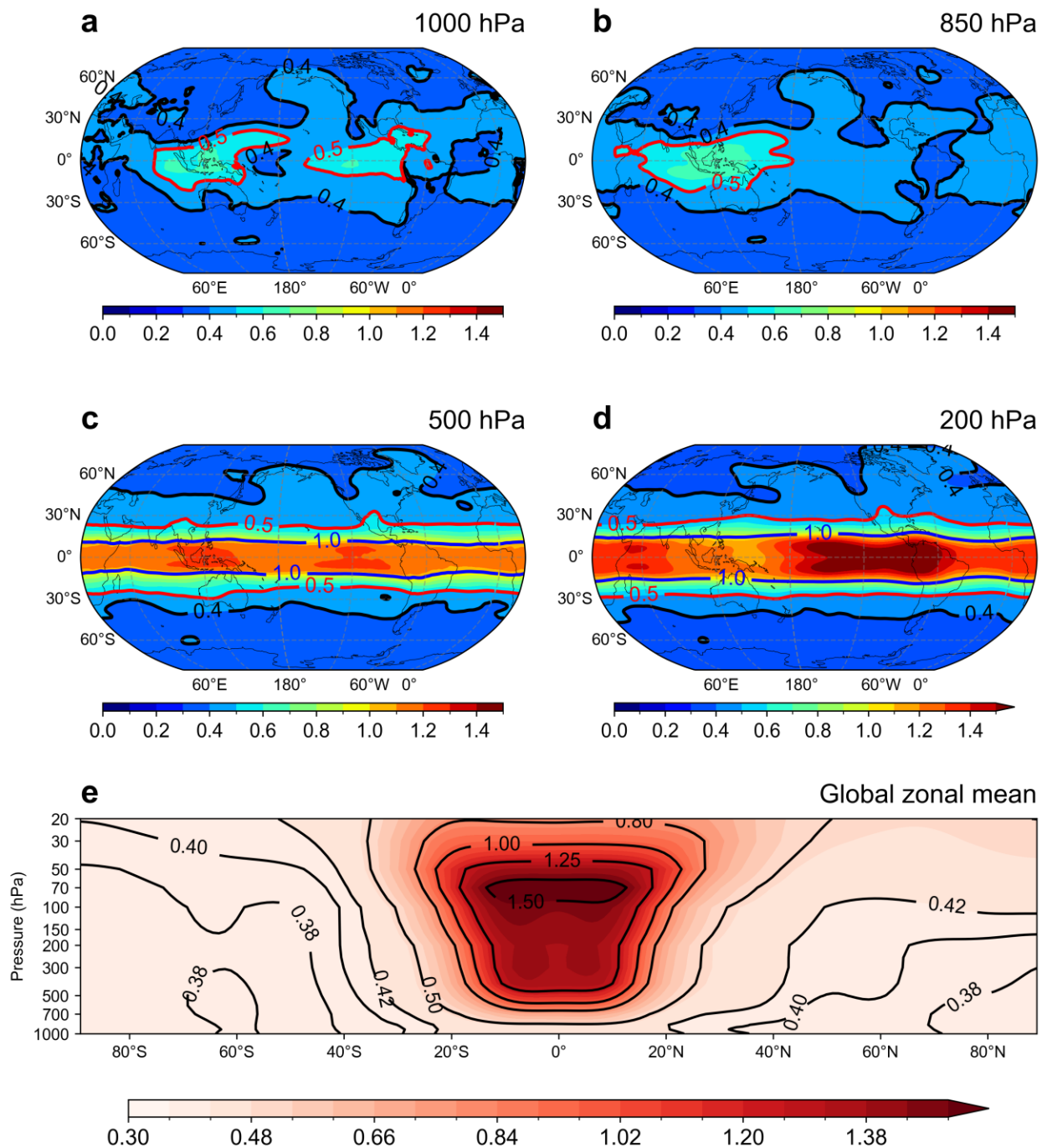


Figure 2. (a–b) The spatial patterns of SNR for geopotential height at the (a) 1000hPa, (b) 850hPa, (c) 500hPa, and (d) 200hPa levels, and (e) vertical distribution of global zonal mean SNR for geopotential height in the Hydra-SINTEX.

4 Mean-states and Variability of SST

Figure 3a–c displays SST climatology in the observations, SINTEX-F and Hydra-SINTEX. The global mean SST of the SINTEX-F and Hydra-SINTEX are approximately 1°C higher than observations (Table S2 in Supporting Information). The positive SST bias exists in both tropical and midlatitude oceans (Figure 3d, e). The models' SST bias is probably due to a combination of spin-up configurations with CO₂ forcing in 2020 and inherent model errors. In addition, prescribing climatological sea ice conditions in the SINTEX-F and Hydra-SINTEX (owing to the lack of the sea ice model) may also contribute to the SST bias. Note that similar SST biases are seen commonly in numerous coupled models and IE experiments (e.g., Zhang et al., 2014). However, the zonally averaged SST exhibits similar meridional distribution among the SINTEX-F, Hydra-SINTEX, and observations (Figure S2 in Supporting Information). In our results, differences in the SST climatology between the SINTEX-F and Hydra-SINTEX are rather small and insignificant globally, indicating notably small AIVs' influences on the SST mean-states (Figure 3f).

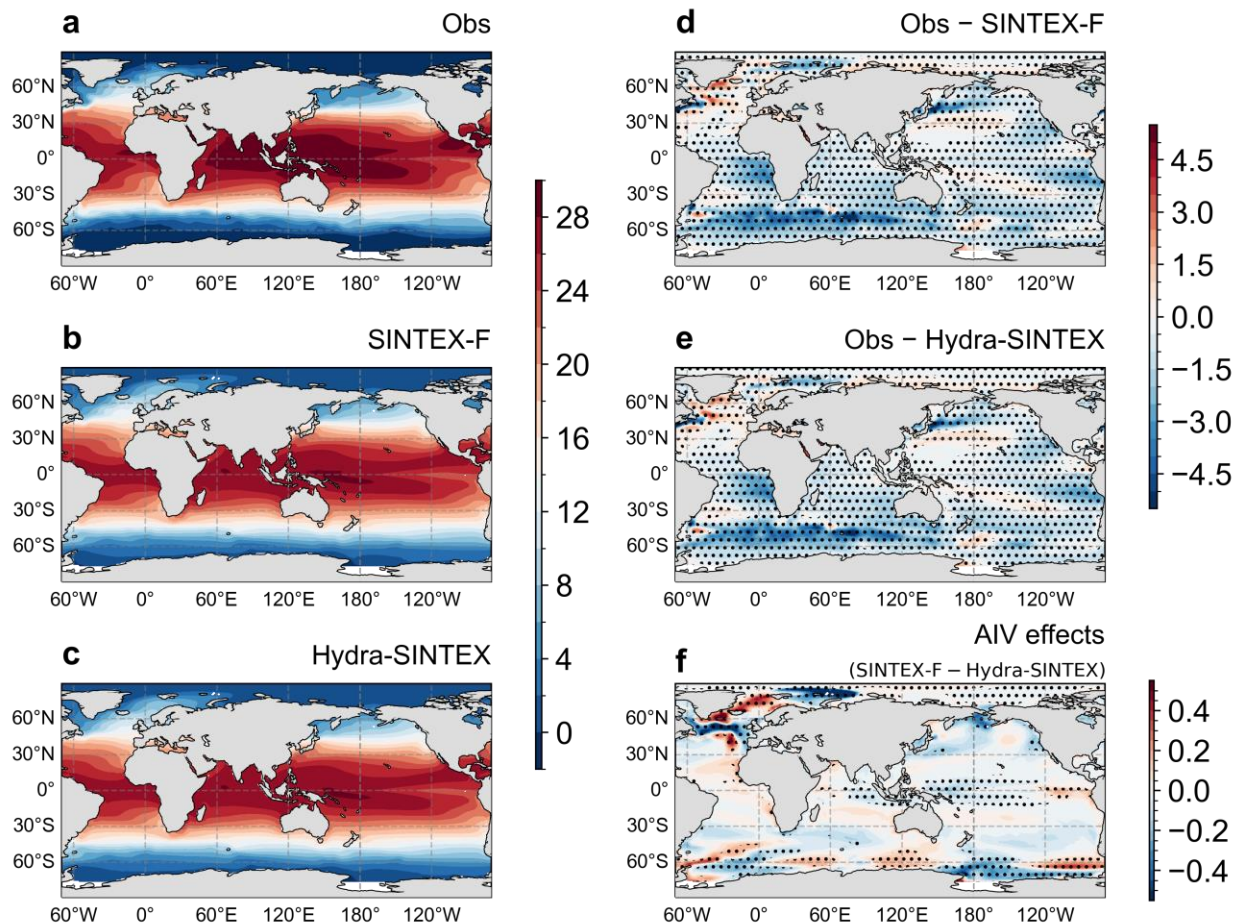


Figure 3. Mean-states of SST (°C) based on (a) the observations, (b) SINTEX-F, and (c) Hydra-SINTEX. (d) Mean-states differences between the observations and SINTEX-F, between the observations and Hydra-SINTEX, and (f) between the SINTEX-F and Hydra-SINTEX. The dots indicate statistically significant at the 95% confidence level based on the student's t-test.

Figure 4 illustrates the variability of SST based on the observation and simulations of the SINTEX-F and Hydra-SINTEX. The SST variability is measured by the standard deviation of monthly mean anomalies (i.e., with the climatological mean seasonal cycle of the 180-year simulations being removed). The outcomes reveal that the SINTEX-F replicates SST variability across many global regions, especially for low-latitudes and mid-latitudes, although there exists a certain degree of weakness. The SINTEX-F exhibits relatively minor discrepancies in SST

variability, primarily noticeable in the Indian Ocean, subtropical North Pacific Ocean, and North Atlantic Ocean (Figure 4b). This alignment provides reliable support for further investigating the role of AIVs on variabilities. However, the SST variability of the Hydra-SINTEX is much weaker than the observation (Figure 4d).

The impact of the AIVs on the SST variability can be estimated with the differences in standard deviations ($\sigma_{\text{diff}} = \sigma_{\text{SINTEX-F}} - \sigma_{\text{Hydra-SINTEX}}$) and reduction rates. We can find large differences in SST variability in the equatorial Pacific Ocean, the tropical eastern Indian Ocean, the subtropical North Pacific Ocean, the Kuroshio–Oyashio extension region, and the North Atlantic Ocean (Figure 4f). The regions with large differences in the SST variability co-occur with strong SST variability, indicating the importance of the AIVs on strong climate signals over the global ocean. However, the reduction rate (Figure 4g) are consistently high (i.e., reduction rate > 0.6) across low latitudes and mid latitudes, with southern hemisphere subtropical oceans experiencing a greater averaged reduction rate. These characteristics are also reflected in zonally averaged profiles of SST variability based on the observations and two model experiments (Figure S3 in Supporting Information).

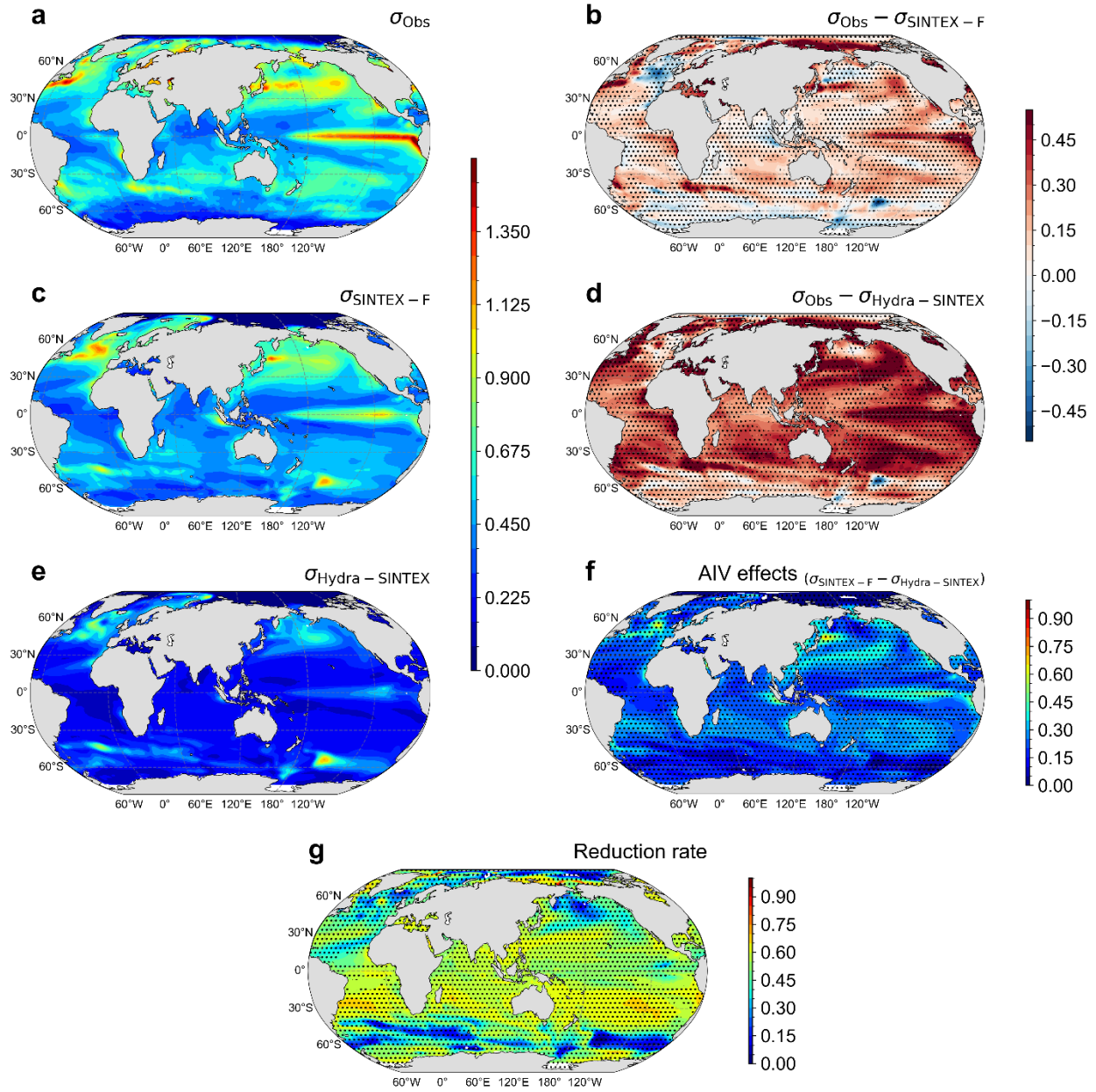


Figure 4. Standard deviations of monthly SST anomalies based on the (a) observations, (c) SINTEX-F, and (e) Hydra-SINTEX, the differences (b) between the observations and SINTEX-F, (d) between the observations and Hydra-SINTEX and (f) between the SINTEX-F and Hydra-SINTEX, and (g) the reduction rate between the SINTEX-F and Hydra-SINTEX. The dots indicate statistically significant at the 95% confidence level based on Levene's test.

5 Impact of the AIVs on the SST Variability

As indicated in the above results, SST variability over many oceanic regions is seen to be strongly influenced by the AIVs, including the equatorial Pacific Ocean, eastern Indian Ocean, and subtropical Northern Pacific Ocean, which are the key regions of well-known climate modes, i.e., ENSO, IOD, Pacific–North American (PNA) teleconnection (Wallace & Gutzler, 1981), Kuroshio–Oyashio front mode (Qiu & Chen, 2010; Qiu & Kelly, 1993), Pacific Meridional Mode (Stuecker, 2018), and North Pacific Oscillation (Di Lorenzo et al., 2008; Zhao et al., 2023). Because AIVs’ influence on ENSO has been thoroughly examined by Kirtman and Shukla (2002), Yeh and Kirtman (2009), and Xin et al. (2014) based on the IE technique, here as two examples, we focus on the eastern Indian Ocean and subtropical North Pacific Ocean.

5.1 SST Variability in the Eastern Indian Ocean

Given the significant impact of AIVs on climate variability in the eastern Indian Ocean, where the observed air–sea coupling is much stronger than that in the western Indian Ocean, we simply measure the IOD with SST anomalies over the tropical eastern Indian Ocean (IODE). In the observations, the IODE is defined as the area spanning from 10°S to 0° and from 90°E to 110°E (Saji et al., 1999). However, like a bias observed in most coupled models, the IOD-related signals in the eastern Indian Ocean extended too far west in the SINTEX-F and Hydra-SINTEX (figure not shown). Due to this, the IODE in simulations is defined as the area spanning from 10°S to 0° and from 85°E to 110°E (Hong, Li, & Luo, 2008). Such a defined IODE index demonstrates a significantly strong negative correlation with the commonly employed Dipole Mode Index (DMI; Saji et al., 1999; Table S3 in Supporting Information), which is derived as differences of SST

anomalies averaged over the western (10°S–10°N, 50°E–70°E) and southeastern Indian Ocean (10°S–0°S, 90°E–110°E).

Based on the IOD index defined in the IODE, positive IOD (pIOD) or negative IOD (nIOD) years are identified when the seasonal mean IOD index in boreal autumn (September–October–November, SON) is above (below) negative (positive) one standard deviation. The other years are classified as normal years. Then, we obtain 32 pIOD events and 35 nIOD events in the 180-year simulation of SINTEX-F, as well as 34 pIOD events and 26 nIOD events in the Hydra-SINTEX. Due to short records of observations, only six pIOD events and three nIOD events are identified (Table S4 in Supporting Information). It indicates that while the frequency of pIOD events does not change much, the total number of nIOD events during the 180-year simulation decreases significantly (from 35 to 26) in the absence of the AIVs.

The differences in the IOD index standard deviations (Figure S4 in Supporting Information) between observations ($\sigma = 0.51$) and the SINTEX-F ($\sigma = 0.61$) are relatively small. However, the standard deviation of the IOD index is reduced to 0.27 after removing the AIVs. The power spectra of unnormalized and normalized IOD indices in the observations, SINTEX-F and Hydra-SINTEX, are depicted in Figure S5 in Supporting Information. In order to generate smoothed power spectra, the 180-year simulations in the SINTEX-F and Hydra-SINTEX are partitioned into three segments of 60 years. Figure S5 represents the power spectra averaged over the three individual segments for both the SINTEX-F and Hydra-SINTEX. The statistical significance of spectral peaks is assessed by comparing them to their respective red noise spectra. The spectral power of unnormalized IOD indices at the interannual time scale is significantly reduced without the AIVs. The power spectrum of the normalized IOD index exhibits notable peaks at the interannual time scale of 1.5–4 years in observations, and 1.2, 3.4–5 years in the SINTEX-F, while

1.3, 1.8–2.2, 4–5 years in the Hydra-SINTEX. Note that the pronounced peak on a nearly 2-year time scale is present in the Hydra-SINTEX, but absent in the observation and SINTEX-F. This biennial periodicity of the IOD is also found in the coupled model sensitivity experiment of Behera et al. (2006). The result implies that air–sea coupling may help generate the biennial periodicity of the IOD, but it can be obscured by the AIVs.

The evolution of the IOD events is well reproduced by the SINTEX-F (Figure S6 in Supporting Information). Note that the model’s bias in the early development stage of nIOD events appears to be larger compared to the pIOD events; this may be partly due to the scarcity of selected nIOD events in observations (only three nIOD events). Nevertheless, intensities for both the pIOD and nIOD events during the peak phase (i.e., SON) are accurately captured in the SINTEX-F. However, after the removal of the AIVs, intensities for both the pIOD and nIOD events during their developing and maturing phases are reduced by 51.3–56.4%. Note that AIVs do not appear to impact the seasonal phase locking of the IOD events (i.e., developing in boreal spring–summer, peaking in SON, and demising rapidly in December).

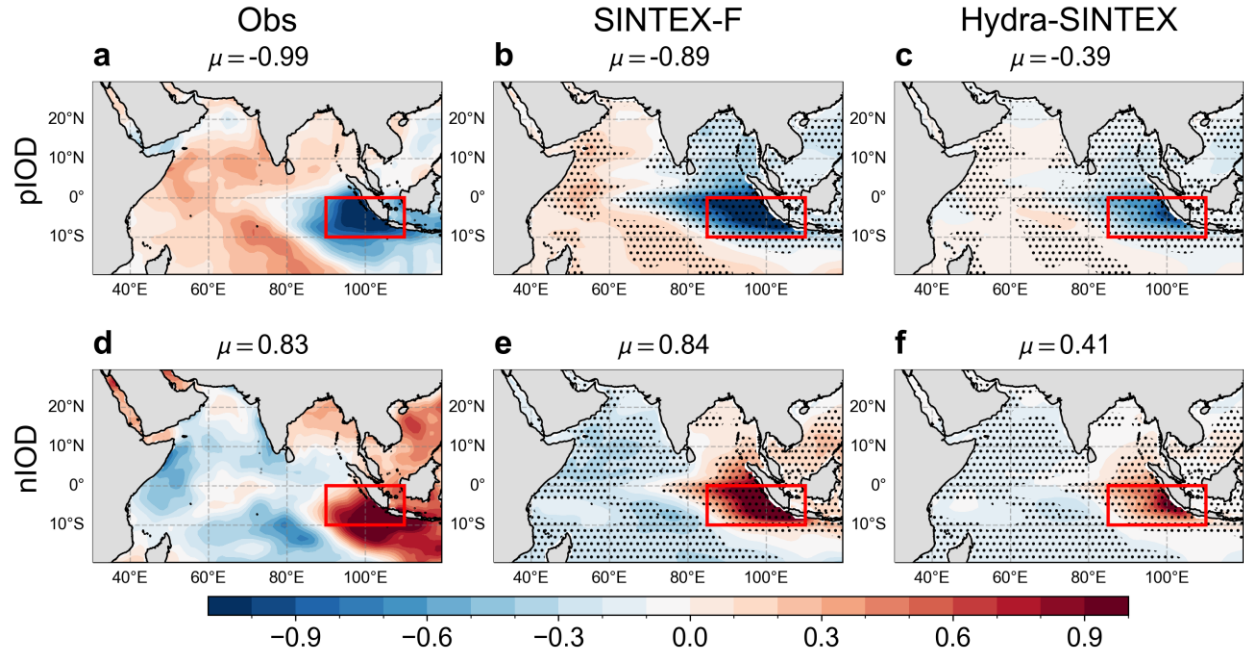


Figure 5. The composite SST anomalies ($^{\circ}\text{C}$) during SON for (a–c) the pIOD and (d–f) nIOD events based on observations (left column), the SINTEX-F (middle column) and Hydra-SINTEX(right column). The red rectangular box in each panel indicates the IODE region for observations and simulations, and μ in the upper center corner of each panel denotes regionally averaged SST anomalies in the IODE region. The dots indicate statistically significant at the 95% confidence level based on the student's t-test.

During the mature phases of pIOD and nIOD events, SST anomalies generally exhibit a symmetrically opposite pattern (albeit with the asymmetry between the intensities of two phases) based on the observations, SINTEX-F and Hydra-SINTEX simulations (Figure 5). However, both pIOD and nIOD intensities in the Hydra-SINTEX are much weaker. Interestingly, SST anomalies related to the IOD are primarily located in the eastern part of the Indian Ocean, i.e., closer to the observations. Unlike results presented in the SINTEX-F (cf. Figures 5c, f and 5b, e), these anomalies do not extend significantly to the west. This suggests that this common model bias may be partly induced by the AIVs.

The inter-event spreads can be measured with the differences among the IOD-related SST variations during SON. The observations display a high spread in the eastern Indian Ocean among the pIOD events ($\sigma = 0.51$), while lower spreads among the nIOD event ($\sigma = 0.18$) (Figure 6, left column). The regions in the eastern Indian Ocean with high spreads among pIOD events are realistically captured by the SINTEX-F, albeit with an underestimation ($\sigma_{\text{obs}} = 0.51$, $\sigma_{\text{SINTEX-F}} = 0.39$; cf. Figure 6a and 6b). For nIOD events, differences in the spreads between the observations and SINTEX-F become much smaller ($\sigma_{\text{obs}} = 0.18$, $\sigma_{\text{SINTEX-F}} = 0.3$; cf. Figure 6d and 6e). However, after the removal of the AIVs, the spreads of pIOD and nIOD events are dramatically reduced, and the spreads become almost identical for pIOD and nIOD events ($\sigma = 0.16$ vs. $\sigma = 0.18$; right column in Figure 6). These results suggest that the AIVs can substantially induce large spreads among the IOD events and the asymmetry of the spreads between pIOD and nIOD events.

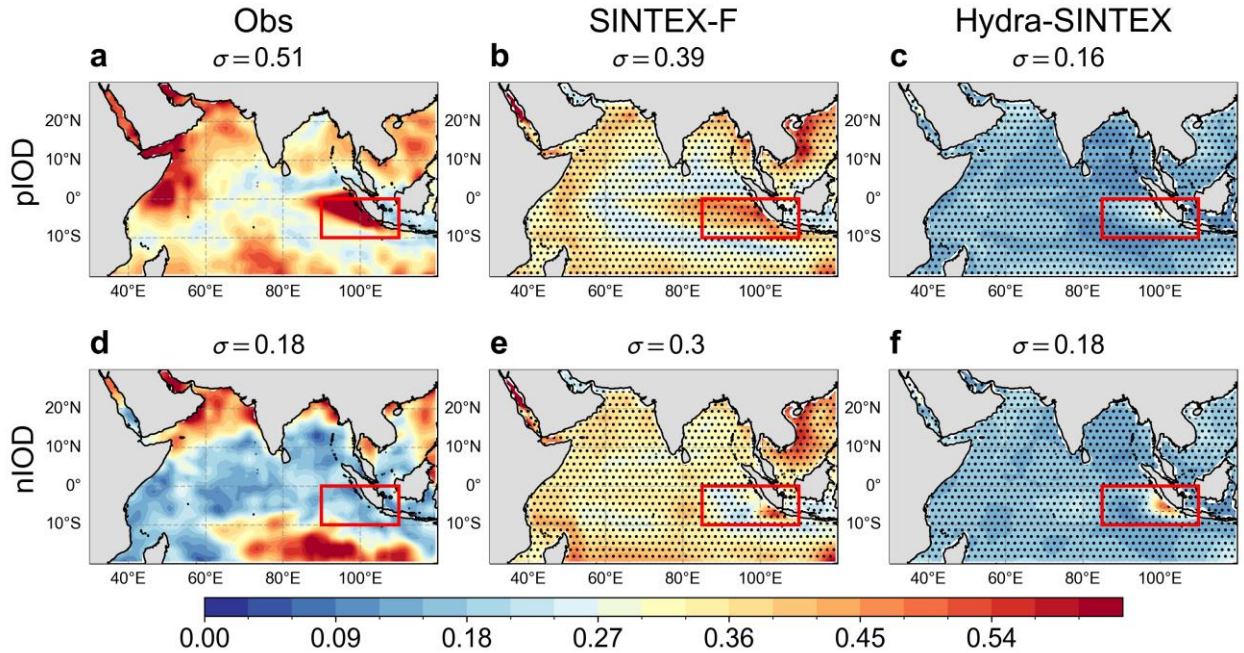


Figure 6. The inter-event spreads of the SST anomalies during SON for (a–c) pIOD and (d–f) nIOD events based on observations (left column), the SINTEX-F (middle column) and Hydra-SINTEX (right column). The red rectangular box in each panel indicates the IODE region for observations and simulations, and σ in the upper center corner of each panel represents regionally averaged inter-event spreads in the IODE region. The dots indicate statistically significant at the 95% confidence level based on Levene’s test.

To enhance comprehension of the AIVs’ impact on IOD events, we conduct a mixed layer heat budget analysis during the IOD’s development phase (i.e., June–September, JJAS; Figure 7a, c). The results indicate that the primary driver of the pIOD and nIOD SST anomalies is oceanic advections in the SINTEX-F and Hydra-SINTEX, while surface heat fluxes mainly serve as a damping factor (see also Neelin et al., 1994 for tropical climate).

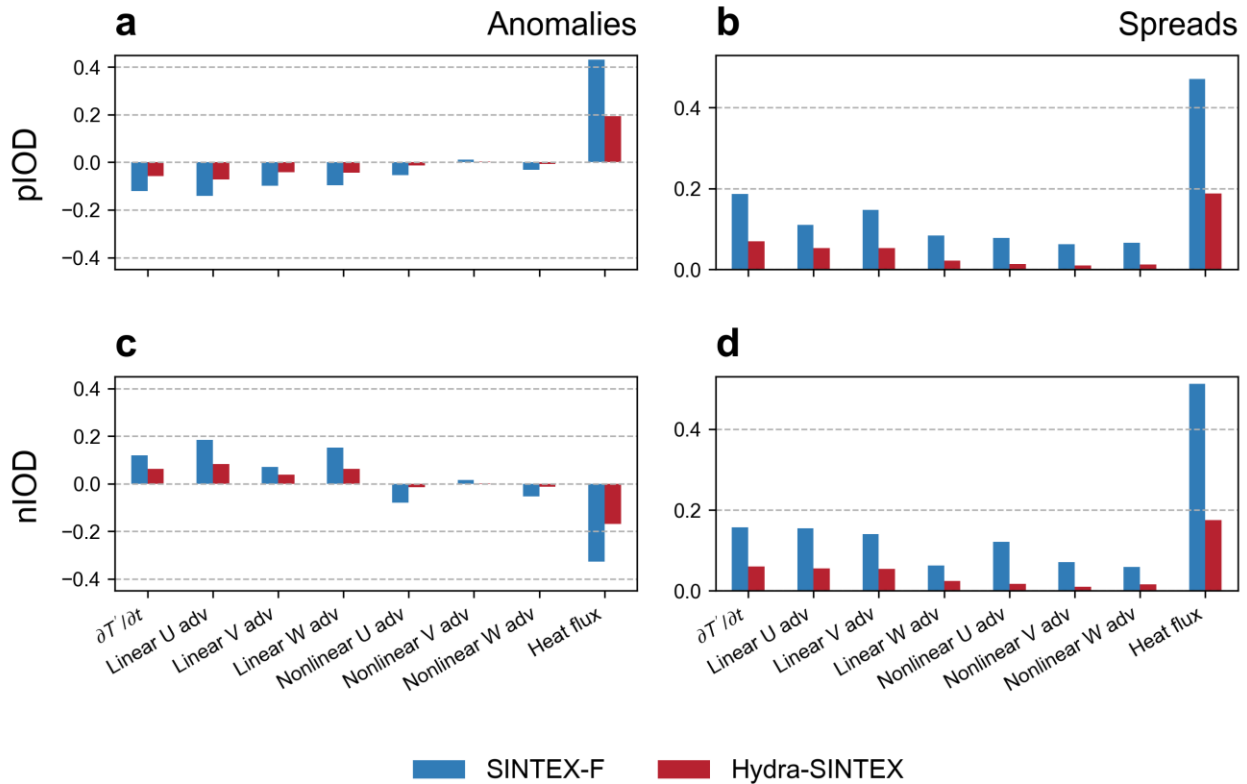


Figure 7. Composite anomalies (left column) and inter-event spreads (right column) for mixed-layer heat budget terms ($^{\circ}\text{C}\cdot\text{month}^{-1}$) in the IODE during JJAS for (a, b) pIOD and (c, d) nIOD events based on the SINTEX-F (blue bars) and Hydra-SINTEX (red bars).

For both pIOD and nIOD events in the SINTEX-F and Hydra-SINTEX, the MLT tendency terms are contributed mainly by linear advection terms. However, nonlinear advection terms act as different roles for different IOD phases, e.g., nonlinear U and W advection terms contribute to the development of pIOD but retard the development of nIOD. After the elimination of the AIVs, MLT tendency terms and linear advection terms decrease by approximately 48–58%, and all nonlinear advection terms are nearly suppressed (Figure 7a, c and Figure S7 in Supporting Information). This accounts for the reduced asymmetry of the IOD events in the Hydra-SINTEX. Consistently, the skewness of the IOD index in the Hydra-SINTEX (-0.02 ; insignificant) is much smaller than that in the SINTEX-F (-0.21 ; significant) (Table S5 in Supporting Information).

We also analyze the inter-event spreads for each mixed layer heat budget term during the development of pIOD and nIOD events (Figure 7b, d). In the SINTEX-F, the spreads of the MLT tendency term ($\sigma = 0.19$) among the pIOD events are slightly larger than that in nIOD events ($\sigma = 0.16$); they are predominantly induced by the high spreads of surface heat flux. In addition, for the pIOD events, the linear U ($\sigma = 0.11$) and V ($\sigma = 0.15$) advection terms are larger than those of the linear W advection term ($\sigma = 0.08$) and the three nonlinear advection terms ($\sigma = 0.06\sim 0.08$). While for the nIOD events, the spreads of the linear U ($\sigma = 0.15$) and V ($\sigma = 0.14$) advection terms and nonlinear U advection terms ($\sigma = 0.12$) highly surpass the other terms. After removing the AIVs, these differences of the spreads between pIOD and nIOD diminish much. The spreads for MLT tendency terms are decreased by approximately 60–67%, leading to almost identical spreads between pIOD ($\sigma = 0.07$) and nIOD ($\sigma = 0.06$). This is consistent with the

differences in the inter-event spreads of the IOD-related SST anomalies during SON (recall Fig. 6).

5.2 SST Variability in the Subtropical North Pacific Ocean

As depicted in Figure 4f, the AIVs not only exert significant effects on tropical SST variability but also exert a substantial impact on the SST variability in the subtropical North Pacific Ocean. The influence is more pronounced during boreal winter (December–January–February, DJF) compared to those in other seasons (Figure S8 in Supporting Information). The maximum differences in the SST variability between the SINTEX-F and Hydra-SINTEX reach up to 0.4°C in the key region (i.e., 30°N – 40°N and 170°W – 150°W) of the subtropical North Pacific Ocean, and corresponding reduction rate is greater than 0.5 (Figure S8a, b). Interestingly, this area almost overlaps with the region (i.e., 26°N – 42°N , 164°W – 148°W ; see Fig. 11 in Alexander et al., 1999) that is used to examine the reemergence (Alexander & Deser, 1995) in the North Pacific Ocean. It suggests that AIVs may have a significant influence on the reemergence of winter SST anomalies in the North Pacific Ocean. In this section, we attempt to analyze AIVs' effects on SST variability during DJF in the subtropical North Pacific Ocean.

In the North Pacific Ocean, the PNA teleconnection mode represents a dominant planetary-scale mid-latitude atmospheric process during the boreal winter (Leathers et al., 1991; Wallace & Gutzler, 1981). It has pronounced influences on the SST variability there (Lau, 1981; Lin & Derome, 1999). Moreover, the influence of ENSO, i.e., the predominant climate mode (Bjerknes, 1969), can extend beyond the tropics, reaching into the North Pacific Ocean to influence SST variability there through the atmospheric bridge (Alexander et al., 2002). Therefore, we will explore the impacts of both the PNA and remote ENSO on the SST variability in the subtropical

North Pacific Ocean. The years of El Niño (La Niña) are identified as the years when the DJF-mean Niño3.4 index reaches one positive (negative) standard deviation. The years when the Niño3.4 index is within ± 1 standard deviation are classified as normal years. A similar way is applied to identify the PNA events as well. Due to constraints imposed by a limited number of observed events, we pay more attention to outcomes derived from the 180-year simulations of the SINTEX-F and Hydra-SINTEX.

Considering that the PNA mode is largely modulated by ENSO (Horel & Wallace, 1981), we undertake an analysis involving pure ENSO events and pure PNA events (Table S6 in Supporting Information). The pure ENSO events encompass El Niño events and La Niña events but with neutral PNA events. In contrast, pure PNA events include positive and negative PNA events but with neutral ENSO signals. Ideally, we can discern the remote impact of ENSO on the subtropical North Pacific Ocean by examining the differences in SST variability, i.e., SINTEX-F minus Hydra-SINTEX, based on pure ENSO events. Similarly, we can isolate the impacts of the mid-latitude atmospheric processes based on pure PNA events.

The spatial patterns of the North Pacific SST anomalies resembling the Pacific Decadal Oscillation (PDO), characterized by a distinctive horseshoe shape, with a focus on the pure ENSO events (Figure 8a, c) and pure PNA events (Figure 8e, g) in the SINTEX-F. This implies that spatial patterns of SST in the North Pacific Ocean could be induced by both remote ENSO and local atmospheric forcing. It shows a positive PDO-like mode (i.e., SST anomalies in the central North Pacific are negative, while positive SST anomalies are observed along the west coast of North America and the eastern tropical Pacific) for both pure El Niño (Figure 8a, b) and pure positive PNA events (Figure 8e, f) in the SINTEX-F and Hydra-SINTEX. On the contrary, both pure La

Niña (Figure 8c, d) and pure negative PNA events (Figure 8g, h) in the SINTEX-F and Hydra-SINTEX show a negative PDO-like mode. However, after suppressing the AIVs, SST anomalies in the pure ENSO events exhibit a significant expansion in the vicinity of the western coast of North America and the eastern tropical Pacific and the SST anomalies in the subtropical North Pacific become rather weak and shrank (Figure 8b, d). In contrast, results based on the pure PNA events of the Hydra-SINTEX exhibit nearly unchanged SST anomaly patterns, albeit with weakened magnitudes (Figure 8f, h), compared to the SINTEX-F. These findings indicate that the AIVs have important roles in shaping the response of SST anomalies in the North Pacific to the remote ENSO forcing.

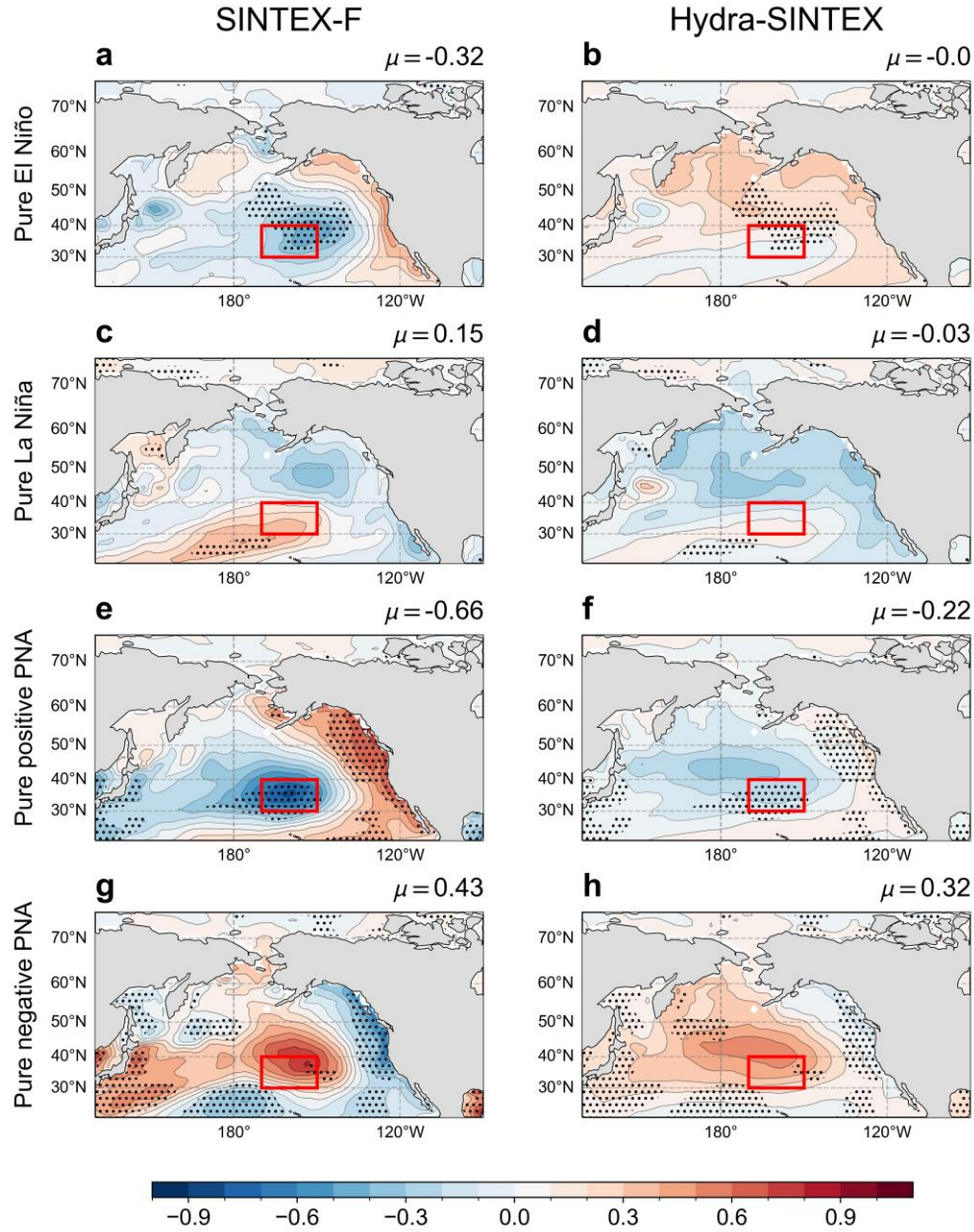


Figure 8. The composite SST anomalies ($^{\circ}\text{C}$) during DJF for (a–b) the pure El Niño, (c–d) pure La Niña, (e–f) pure positive PNA, and (g–h) pure negative PNA events based on the SINTEX-F (left column), and Hydra-SINTEX (right column). The red rectangular box in each panel indicates the target region (i.e., 30°N – 40°N and 170°W – 150°W), and the μ value in the upper right corner of each panel denotes the regionally averaged SST anomalies in the target region. The dots indicate statistically significant at the 95% confidence level based on the student's t-test.

We also analyze the effects on the SST variability by mid-latitude atmospheric processes and remote ENSO based on the four categories in the subtropical North Pacific Ocean (Figure 9). In the SINTEX-F model simulations, intensities of SST variability during pure ENSO and pure PNA events are similar ($\sigma = 0.55 \sim 0.62$, left column in Figure 9), indicating more or less comparable impacts of remote ENSO and local atmospheric forcing. After suppressing the AIVs, the SST variabilities there for all four categories are much reduced but with different reductions (middle and right column in Figure 9). The findings indicate a more pronounced decrease in SST variabilities within the subtropical North Pacific when experiencing pure negative PNA and pure El Niño cases ($\sigma_{\text{diff}} = 0.43$ and 0.37), as opposed to pure La Niña and pure positive PNA cases ($\sigma_{\text{diff}} = 0.25$ and 0.29). This suggests a nonlinear feature induced by the AIVs regarding the impacts of the mid-latitude atmospheric processes and remote ENSO on the SST variability in the North Pacific. This nonlinear feature between the pure El Niño and La Niña cases (i.e., $0.37 - 0.25 = 0.12$) is similar to that between the pure positive and negative PNA cases (i.e., $0.43 - 0.29 = 0.14$). The current findings exhibit some discrepancies when compared to the studies of Yeh and Kirtman (2004) and Yeh et al. (2007), which underscored the significance of mid-latitude atmospheric processes in influencing SST variability in the central North Pacific region.

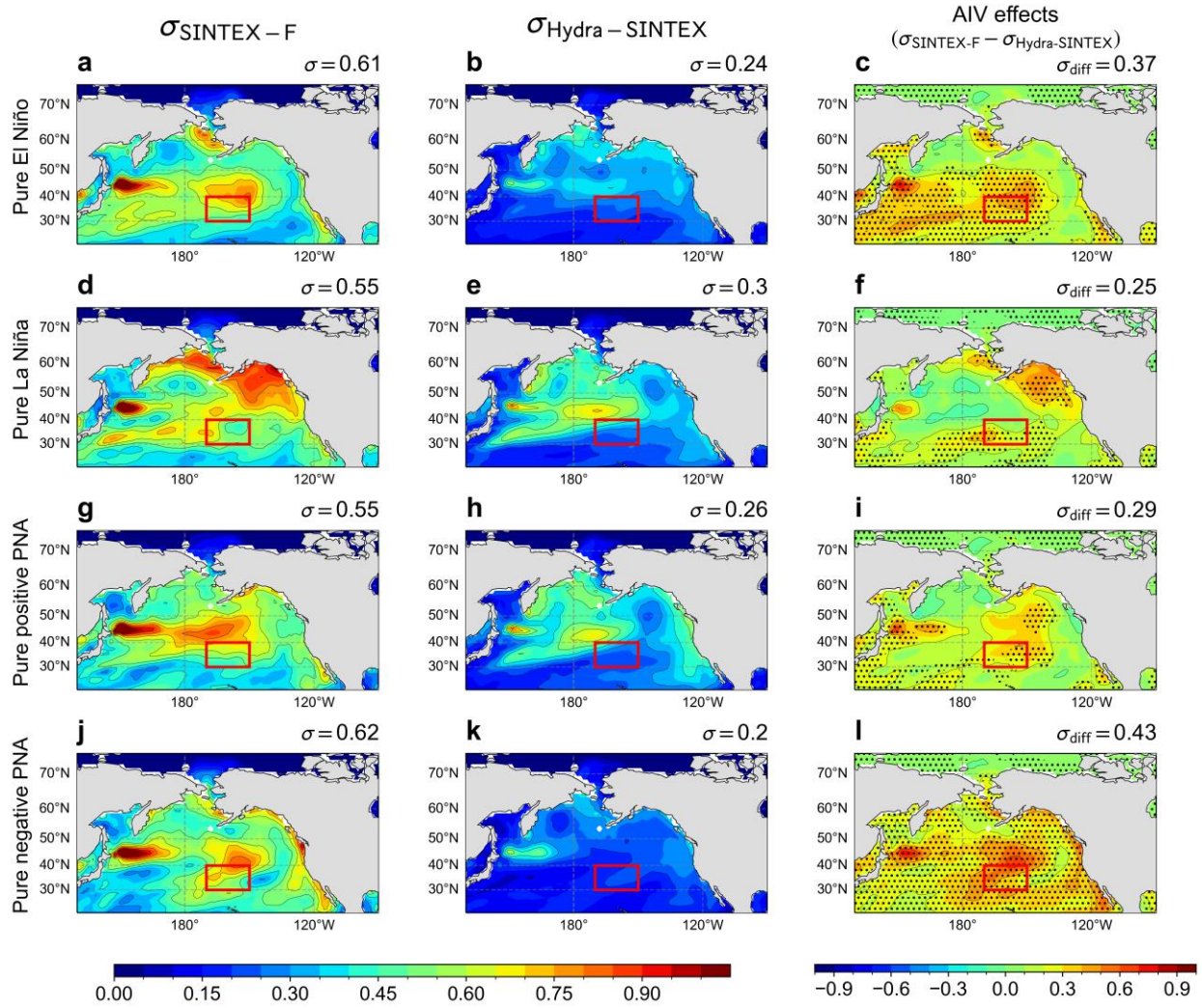


Figure 9. The standard deviations of monthly SST anomalies during DJF for (a–c) pure El Niño, (d–f) pure La Niña, (g–i) pure positive PNA, and (j–l) pure negative PNA events based on the SINTEX-F (left column), Hydra-SINTEX (middle column) and the differences between the SINTEX-F and Hydra-SINTEX (right column). The red rectangular box in each panel indicates the target region, and the σ value in the upper right corner of each panel denotes the regionally averaged standard deviations of the SST anomalies in the target region. The dots indicate statistically significant at the 95% confidence level based on Levene's test.

To understand the mechanisms underlying SST anomalies in the subtropical North Pacific Ocean, we further analyze the mixed layer heat budget for pure ENSO and pure PNA cases (Figure

10a, c, e, g). For the cases of negative MLT tendency (i.e., pure El Niño and pure positive PNA cases; Figure 10a, e), distinctions mainly arise from the linear V and linear W advection term between the SINTEX-F and Hydra-SINTEX. The linear V advection term is larger in pure positive PNA ($-0.15\text{ }^{\circ}\text{C}\cdot\text{month}^{-1}$) than pure El Niño ($-0.08\text{ }^{\circ}\text{C}\cdot\text{month}^{-1}$) cases in the SINTEX-F. After the removal of AIVs, the reduction in linear V advection term in pure El Niño cases (89.34%) is greater than that in pure positive PNA cases (56.59%). The linear W advection term contributes positively in pure El Niño cases but negatively in pure positive PNA cases. However, the values of linear W advection are of opposite signs between the SINTEX-F and Hydra-SINTEX for both pure El Niño and pure positive PNA cases, indicating strong effects of AIVs on linear W advection term.

As for the cases of positive MLT tendency, primary contributors for pure La Niña and pure negative PNA cases are different (Figure 10c, g). The positive MLT tendency term is mainly attributed by the linear W advection term ($0.11\text{ }^{\circ}\text{C}\cdot\text{month}^{-1}$) and surface heat flux term ($0.08\text{ }^{\circ}\text{C}\cdot\text{month}^{-1}$) in pure La Niña cases, while the linear V advection term ($0.25\text{ }^{\circ}\text{C}\cdot\text{month}^{-1}$) plays a dominant role in pure negative PNA cases. With the elimination of the AIVs, the linear W advection term becomes nearly zero ($0.01\text{ }^{\circ}\text{C}\cdot\text{month}^{-1}$), and the surface heat flux term ($0.04\text{ }^{\circ}\text{C}\cdot\text{month}^{-1}$) is reduced by 53% for pure La Niña cases. For pure negative PNA cases, the linear V advection term ($0.07\text{ }^{\circ}\text{C}\cdot\text{month}^{-1}$) is reduced by 70%.

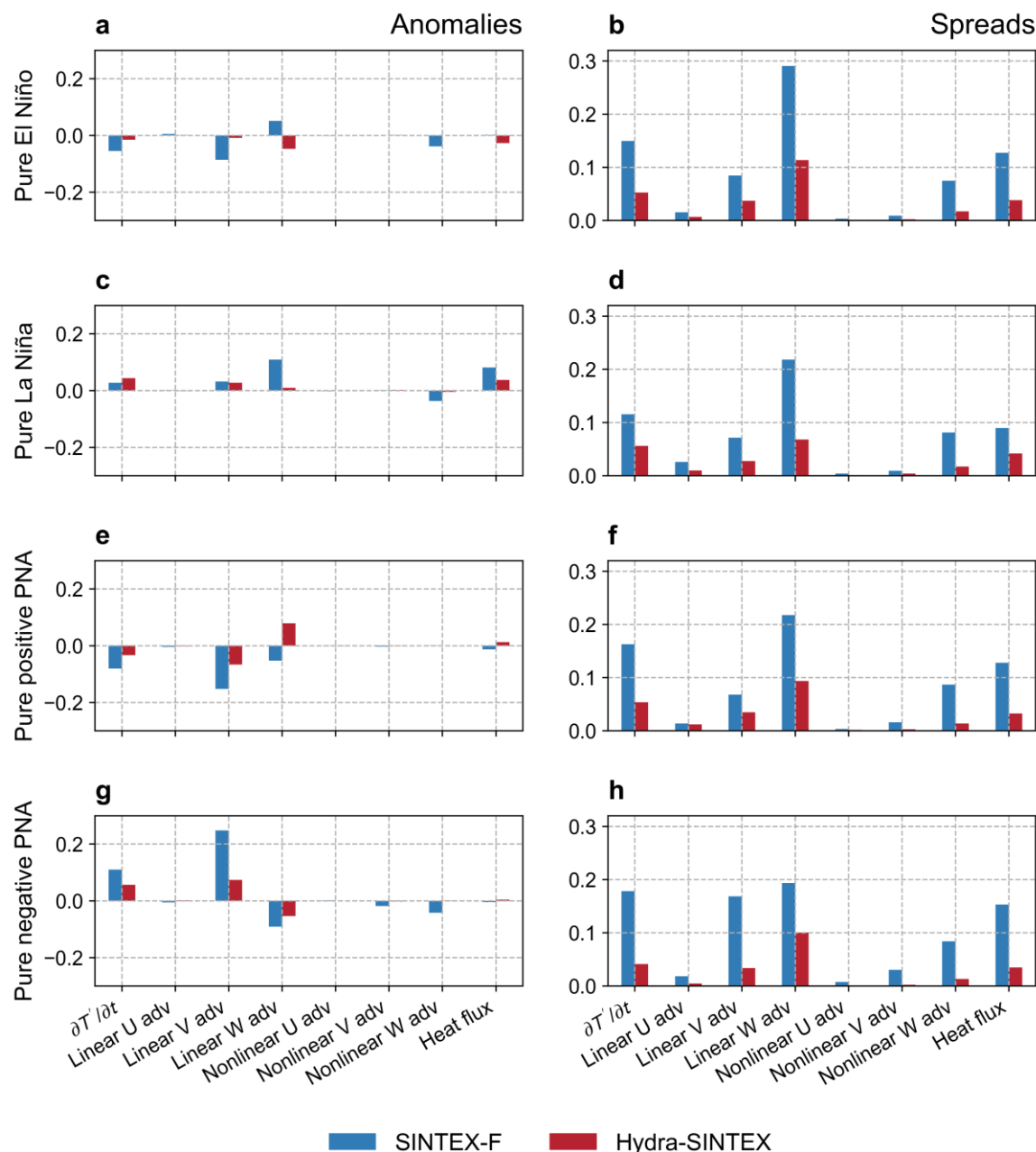


Figure 10. The composite anomalies (left column) and spreads (right column) of six mixed-layer heat budget terms ($^{\circ}\text{C}\cdot\text{month}^{-1}$) in the target region (i.e., 30°N - 40°N and 170°W - 150°W) during DJF for (a–b) pure El Niño, (c–d) pure La Niña, (e–f) pure positive PNA, and (g–h) pure negative PNA events based on the SINTEX-F (blue bars) and Hydra-SINTEX (red bars).

We also analyze the spreads of each mixed layer heat budget term in the subtropical North Pacific for pure ENSO and PNA cases (Figure 10b, d, f, h). The spreads of MLT tendency term are comparable between ENSO and PNA cases in the SINTEX-F ($\sigma = 0.12\sim 0.18$) but much reduced in the Hydra-SINTEX ($\sigma = 0.04\sim 0.05$), suggesting a strong influence of AIVs. Among all terms, the linear W advection term displays the highest spreads for all four cases ($\sigma = 0.19\sim 0.29$). After the removal of the AIVs, the spreads of linear W advection term decrease by 48.03~68.97%, but their spreads are still the highest ($\sigma = 0.06\sim 0.11$) among all terms. Note that the reduction rate after removing AIVs varies among different heat budget terms and different ENSO and PNA cases, implying different impacts of AIVs on different processes and cases.

6 Summary and Discussions

The climate is an intricate system involving a multitude of processes that function across diverse spatial and temporal scales (e.g., Rind, 1999). The atmospheric and oceanic processes and their interactions have significant impacts on climate variabilities on Earth. The SST, which is highly predictable and acts as a vital boundary forcing to the atmosphere, has strong influences on global climate and weather events. In addition, atmospheric internal signals, which exhibit noisy and unpredictable characteristics in general, can also have a potential impact on climate variabilities. To elucidate the potential influence of AIVs on climate variabilities, we adopt the concept of the IE (Kirtman & Shukla, 2002) to formulate an interactive ensemble model (i.e., Hydra-SINTEX) based on the standard coupled SINTEX-F model.

Based on the 180-year simulations of the SINTEX-F and Hydra-SINTEX models, we find that the AIVs exert minimal influence on the global mean-state of SST, with only minimal impacts on both the magnitude and spatial distribution. However, the AIVs significantly influence the SST

variability in many regions, notably the tropical eastern Indian Ocean, equatorial Pacific, subtropical North Pacific, and the North Atlantic. These regions correspond to the primary areas associated with various established climate modes. In this study, we mainly pay attention to SST variability in two regions, that is, the tropical eastern Indian Ocean, which holds a central position in the IOD, and the subtropical North Pacific where both mid-latitude atmosphere processes and remote ENSO influence are important. Our results show that, when the AIVs are suppressed, there is a significant reduction of over 50% in the intensity of the IOD, the inter-event spreads of the IOD, and the asymmetry between pIOD and nIOD events. And the notable decrease of SST variability in the subtropical North Pacific Ocean is jointly caused by the weakened influence from mid-latitude atmospheric processes and remote ENSO.

In summary, our results indicate the great importance of atmospheric internal high-frequency signals in generating low-frequency SST variability, consistent with previous studies (e.g., Kirtman & Shukla, 2002; Yeh & Kirtman, 2009). In many respects, this presents formidable challenges in simulating and forecasting climate variations, given the inherently unpredictable characteristics of the AIVs (e.g., Lorenz, 1963; Jain et al., 2023; Mitchell et al., 2013; Deser et al., 2012). While the IE framework can overcome the limitations imposed by observational data, offering a valuable approach to achieving an in-depth understanding of the thermodynamic and dynamic mechanisms linked to the influence of AIVs on climate variabilities, we need to find effective methods to improve climate simulations and predictions. One potential solution entails adopting the super-model framework (Selten et al., 2011; van den Berge et al., 2011) instead of the prevalent multi-model ensembles (MMEs) approach (Doblas-Reyes et al., 2000; Houtekamer et al., 1996; Krishnamurti et al., 1999). The super-model strategy facilitates the exchange of information among models during the simulation process, as opposed to combining the outcomes

derived from the individual models afterward. This approach has been preliminarily demonstrated to significantly improve the simulation of ocean–atmosphere interactions and climate (e.g., Counillon et al., 2023; Shen et al., 2016). This justifies the need for ongoing dedication in the coming years.

Acknowledgments

This work is supported by National Natural Science Foundation of China (Grant No. 42030605 and 42088101) and National Key R&D Program of China (Grant No. 2020YFA0608000). The model simulation takes place at the High Performance Computing Center of Nanjing University of Information Science and Technology. Additionally, The data in this study are analyzed and plotted by the Climate Data Operators v2.2.0 (<https://code.mpimet.mpg.de/projects/cdo>), Python v3.10 software (<https://www.python.org/downloads/release/python-3100/>) with the packages of the numpy (Harris et al., 2020), xarray (Hoyer & Hamman, 2017), dask (<https://www.dask.org>), matplotlib Hunter, 2007, cartopy (<https://scitools.org.uk/cartopy>), scipy (Virtanen et al., 2020), easyclimate (Shenyulu, 2024), xeofs (Rieger & Levang, 2024), and REDFIT Version 3.8e software (Schulz & Mudelsee, 2002, <https://www.marum.de/Prof.-Dr.-michael-schulz/Michael-Schulz-Software.html>) for power spectra analysis. We wish to extend our sincere appreciation to Shanshan Liu, Yue Li, Jiaqing Xue, and Jiuwei Zhao for their invaluable constructive comments. Additionally, we express our gratitude to the three anonymous reviewers whose insightful comments and constructive suggestions have significantly helped improve this manuscript.

Conflict of Interest

The authors disclose that there are no conflicts of interest pertinent to this research.

Data Availability Statements

You can locate the observation and model data in the following source:

The SINTEX-F and Hydra-SINTEX-F model dataset used in this study is available on Figshare (Zhang, 2024a, 2024b) via <https://doi.org/10.6084/m9.figshare.24978633.v2> and <https://doi.org/10.6084/m9.figshare.24978648.v3>, reinforcing the availability of the data that underpins the findings in this article. The Global Monitoring Laboratory (GML) dataset used for transient carbon dioxide observational data in the study are available at NOAA Global Monitoring Laboratory via <https://www.gml.noaa.gov>. The Optimum Interpolation Sea Surface Temperature (OISST) dataset employed for the sea surface temperature data can be accessed through the NCEI via <https://www.ncei.noaa.gov/products/optimum-interpolation-sst>. The ERA5 datasets employed for the 500-hPa geopotential height in the research are accessible through the Climate Data Store via <https://confluence.ecmwf.int/display/CKB/The+family+of+ERA5+datasets>.

References

Alexander, M. A., Bladé, I., Newman, M., Lanzante, J. R., Lau, N.-C., & Scott, J. D. (2002). The Atmospheric Bridge: The Influence of ENSO Teleconnections on Air–Sea Interaction over the Global Oceans. *Journal of Climate*, 15(16), 2205-2231. [https://doi.org/10.1175/1520-0442\(2002\)015<2205:TABTIO>2.0.CO;2](https://doi.org/10.1175/1520-0442(2002)015<2205:TABTIO>2.0.CO;2)

Alexander, M. A., & Deser, C. (1995). A Mechanism for the Recurrence of Wintertime Midlatitude SST Anomalies. *Journal of Physical Oceanography*, 25(1), 122-137. [https://doi.org/10.1175/1520-0485\(1995\)025<0122:AMFTRO>2.0.CO;2](https://doi.org/10.1175/1520-0485(1995)025<0122:AMFTRO>2.0.CO;2)

Alexander, M. A., Deser, C., & Timlin, M. S. (1999). The Reemergence of SST Anomalies in the North Pacific Ocean. *Journal of Climate*, 12(8), 2419-2433. [https://doi.org/10.1175/1520-0442\(1999\)012<2419:TROSAI>2.0.CO;2](https://doi.org/10.1175/1520-0442(1999)012<2419:TROSAI>2.0.CO;2)

- Argüeso, D., Romero, R., & Homar, V. (2020). Precipitation Features of the Maritime Continent in Parameterized and Explicit Convection Models. *Journal of Climate*, 33(6), 2449-2466. <https://doi.org/10.1175/JCLI-D-19-0416.1>
- Bamston, A. G., Chelliah, M., & Goldenberg, S. B. (1997). Documentation of a highly ENSO-related sst region in the equatorial pacific: Research note. *Atmosphere-Ocean*, 35(3), 367-383. <https://doi.org/10.1080/07055900.1997.9649597>
- Barnston, A. G., & Livezey, R. E. (1987). Classification, Seasonality and Persistence of Low-Frequency Atmospheric Circulation Patterns. *Monthly Weather Review*, 115(6), 1083-1126. [https://doi.org/10.1175/1520-0493\(1987\)115<1083:CSAPOL>2.0.CO;2](https://doi.org/10.1175/1520-0493(1987)115<1083:CSAPOL>2.0.CO;2)
- Behera, S. K., Luo, J. J., Masson, S., Rao, S. A., Sakuma, H., & Yamagata, T. (2006). A CGCM Study on the Interaction between IOD and ENSO. *Journal of Climate*, 19(9), 1688-1705. <https://doi.org/10.1175/JCLI3797.1>
- Bjerknes, J. (1969). Atmospheric teleconnections from the equatorial Pacific. *Monthly Weather Review*, 97(3), 163-172. [https://doi.org/10.1175/1520-0493\(1969\)097<0163:ATFTEP>2.3.CO;2](https://doi.org/10.1175/1520-0493(1969)097<0163:ATFTEP>2.3.CO;2)
- Brown, M. B., & Forsythe, A. B. (1974). Robust Tests for the Equality of Variances. *Journal of the American Statistical Association*, 69(346), 364-367. <https://doi.org/10.1080/01621459.1974.10482955>
- Capotondi, A., McGregor, S., McPhaden, M. J., Cravatte, S., Holbrook, N. J., Imada, Y., . . . Xu, T. (2023). Mechanisms of tropical Pacific decadal variability. *Nature Reviews Earth & Environment*, 4(11), 754-769. <https://doi.org/10.1038/s43017-023-00486-x>

Counillon, F., Keenlyside, N., Wang, S., Devilliers, M., Gupta, A., Koseki, S., & Shen, M.-L. (2023). Framework for an Ocean-Connected Supermodel of the Earth System. *Journal of Advances in Modeling Earth Systems*, 15(3), e2022MS003310. <https://doi.org/https://doi.org/10.1029/2022MS003310>

Deser, C., Knutti, R., Solomon, S., & Phillips, A. S. (2012). Communication of the role of natural variability in future North American climate. *Nature Climate Change*, 2(11), 775-779. <https://doi.org/10.1038/nclimate1562>

Deser, C., Phillips, A. S., Alexander, M. A., & Smoliak, B. V. (2014). Projecting North American Climate over the Next 50 Years: Uncertainty due to Internal Variability. *Journal of Climate*, 27(6), 2271-2296. <https://doi.org/10.1175/JCLI-D-13-00451.1>

Deser, C., Phillips, A. S., & Hurrell, J. W. (2004). Pacific Interdecadal Climate Variability: Linkages between the Tropics and the North Pacific during Boreal Winter since 1900. *Journal of Climate*, 17(16), 3109-3124. [https://doi.org/10.1175/1520-0442\(2004\)017<3109:PICVLB>2.0.CO;2](https://doi.org/10.1175/1520-0442(2004)017<3109:PICVLB>2.0.CO;2)

Di Lorenzo, E., Schneider, N., Cobb, K. M., Franks, P. J. S., Chhak, K., Miller, A. J., . . . Rivière, P. (2008). North Pacific Gyre Oscillation links ocean climate and ecosystem change. *Geophysical Research Letters*, 35(8). <https://doi.org/10.1029/2007GL032838>

Doblas-Reyes, F. J., Déqué, M., & Pielikev, J.-P. (2000). Multi-model spread and probabilistic seasonal forecasts in PROVOST. *Quarterly Journal of the Royal Meteorological Society*, 126(567), 2069-2087. <https://doi.org/https://doi.org/10.1002/qj.49712656705>

658 Erjavec, N. (2011). Tests for Homogeneity of Variance. In M. Lovric (Ed.), *International*
 659 *Encyclopedia of Statistical Science* (pp. 1595-1596). Springer Berlin Heidelberg.
 660 https://doi.org/10.1007/978-3-642-04898-2_590

661 Fueglistaler, S., Dessler, A. E., Dunkerton, T. J., Folkins, I., Fu, Q., & Mote, P. W. (2009).
 662 Tropical tropopause layer. *Reviews of Geophysics*, 47(1).
 663 <https://doi.org/https://doi.org/10.1029/2008RG000267>

664 Garfinkel, C. I., Gerber, E. P., Paldor, N., & Shamir, O. (2023). The Matsuno–Gill model
 665 on the sphere. *Journal of Fluid Mechanics*, 964, A32, Article A32.
 666 <https://doi.org/10.1017/jfm.2023.369>

667 Gill, A. E. (1980). Some simple solutions for heat-induced tropical circulation. *Quarterly*
 668 *Journal of the Royal Meteorological Society*, 106(449), 447-462.
 669 <https://doi.org/https://doi.org/10.1002/qj.49710644905>

670 Gualdi, S., Navarra, A., Guilyardi, E., & Delecluse, P. (2003). Assessment of the tropical
 671 Indo-Pacific climate in the SINTEX CGCM. *Annals of Geophysics*. [https://doi.org/10.4401/ag-](https://doi.org/10.4401/ag-3385)
 672 3385

673 Hannachi, A. (2001). Toward a Nonlinear Identification of the Atmospheric Response to
 674 ENSO. *Journal of Climate*, 14(9), 2138-2149. [https://doi.org/10.1175/1520-](https://doi.org/10.1175/1520-0442(2001)014<2138:TANIOT>2.0.CO;2)
 675 0442(2001)014<2138:TANIOT>2.0.CO;2

676 Harris, C. R., Millman, K. J., van der Walt, S. J., Gommers, R., Virtanen, P., Cournapeau,
 677 D., . . . Oliphant, T. E. (2020). Array programming with NumPy [Software]. *Nature*, 585(7825),
 678 357-362. <https://doi.org/10.1038/s41586-020-2649-2>

Hasselmann, K. (1976). Stochastic climate models Part I. Theory. *Tellus*, 28(6), 473-485.
<https://doi.org/https://doi.org/10.1111/j.2153-3490.1976.tb00696.x>

He, J., Luo, J.-J., Doi, T., Liu, S., Tang, S., & Wang, X. (2023). Understanding extremely
pluvial winters over Yangtze–Huia river basin in China: their complexity and tropical oceans
influences. *Climate Dynamics*, 61(1), 687-707. <https://doi.org/10.1007/s00382-022-06614-5>

He, J., Wu, J., & Luo, J.-J. (2020). Introduction to climate forecast system version 1.0 of
Nanjing University of Information Science and Technology. *Trans Atmos Sci*, 43(1), 128-143.
<https://doi.org/10.13878/j.cnki.dqkxxb.20191110007>

Hersbach, H., Bell, B., Berrisford, P., Hirahara, S., Horányi, A., Muñoz-Sabater, J., . . .
Thépaut, J.-N. (2020). The ERA5 global reanalysis [Dataset]. *Quarterly Journal of the Royal
Meteorological Society*, 146(730), 1999-2049. <https://doi.org/https://doi.org/10.1002/qj.3803>

Hoerling, M. P., Kumar, A., & Zhong, M. (1997). El Niño, La Niña, and the Nonlinearity
of Their Teleconnections. *Journal of Climate*, 10(8), 1769-1786. [https://doi.org/10.1175/1520-0442\(1997\)010<1769:ENOLNA>2.0.CO;2](https://doi.org/10.1175/1520-0442(1997)010<1769:ENOLNA>2.0.CO;2)

Hong, c.-c., Li, T., Linho, & Kug, J. S. (2008). Asymmetry of the Indian Ocean Dipole.
Part I: Observational Analysis. *Journal of Climate - J CLIMATE*, 21, 4834-4848.
<https://doi.org/10.1175/2008JCLI2222.1>

Hong, C.-C., Li, T., & Luo, J.-J. (2008). Asymmetry of the Indian Ocean Dipole. Part II:
Model Diagnosis. *Journal of Climate*, 21(18), 4849-4858.
<https://doi.org/10.1175/2008JCLI2223.1>

Horel, J. D., & Wallace, J. M. (1981). Planetary-Scale Atmospheric Phenomena Associated with the Southern Oscillation. *Monthly Weather Review*, 109(4), 813-829. [https://doi.org/10.1175/1520-0493\(1981\)109<0813:PSAPAW>2.0.CO;2](https://doi.org/10.1175/1520-0493(1981)109<0813:PSAPAW>2.0.CO;2)

Houtekamer, P. L., Lefaivre, L., Derome, J., Ritchie, H., & Mitchell, H. L. (1996). A System Simulation Approach to Ensemble Prediction. *Monthly Weather Review*, 124(6), 1225-1242. [https://doi.org/10.1175/1520-0493\(1996\)124<1225:ASSATE>2.0.CO;2](https://doi.org/10.1175/1520-0493(1996)124<1225:ASSATE>2.0.CO;2)

Hoyer, S., & Hamman, J. (2017). xarray: N-D labeled Arrays and Datasets in Python [Software]. *Journal of Open Research Software*. <https://doi.org/10.5334/jors.148>

Hu, Z.-Z., Kumar, A., & Zhu, J. (2021). Dominant modes of ensemble mean signal and noise in seasonal forecasts of SST. *Climate Dynamics*, 56(3), 1251-1264. <https://doi.org/10.1007/s00382-020-05531-9>

Huang, B., Liu, C., Banzon, V., Freeman, E., Graham, G., Hankins, B., . . . Zhang, H.-M. (2021). Improvements of the Daily Optimum Interpolation Sea Surface Temperature (DOISST) Version 2.1 [Dataset]. *Journal of Climate*, 34(8), 2923-2939. <https://doi.org/10.1175/JCLI-D-20-0166.1>

Hunter, J. D. (2007). Matplotlib: A 2D Graphics Environment [Software]. *Computing in Science & Engineering*, 9(3), 90-95. <https://doi.org/10.1109/MCSE.2007.55>

Izumo, T., Vialard, J., Lengaigne, M., & Suresh, I. (2020). Relevance of Relative Sea Surface Temperature for Tropical Rainfall Interannual Variability. *Geophysical Research Letters*, 47(3), e2019GL086182. <https://doi.org/10.1029/2019GL086182>

Jain, S., Scaife, A. A., Shepherd, T. G., Deser, C., Dunstone, N., Schmidt, G. A., . . .
Turkington, T. (2023). Importance of internal variability for climate model assessment. *npj
Climate and Atmospheric Science*, 6(1), 68. <https://doi.org/10.1038/s41612-023-00389-0>

Kirtman, B. P., & Shukla, J. (2002). Interactive coupled ensemble: A new coupling strategy
for CGCMs. *Geophysical Research Letters*, 29(10), 5-1-5-4.
<https://doi.org/10.1029/2002GL014834>

Kirtman, B. P., Straus, D. M., Min, D., Schneider, E. K., & Siqueira, L. (2009). Toward
linking weather and climate in the interactive ensemble NCAR climate model. *Geophysical
Research Letters*, 36(13). <https://doi.org/10.1029/2009GL038389>

Krishnamurti, T. N., Kishtawal, C. M., LaRow, T. E., Bachiochi, D. R., Zhang, Z.,
Williford, C. E., . . . Surendran, S. (1999). Improved Weather and Seasonal Climate Forecasts from
Multimodel Superensemble. *Science*, 285(5433), 1548-1550.
<https://doi.org/10.1126/science.285.5433.1548>

Kumar, A., & Hoerling, M. P. (2000). Analysis of a Conceptual Model of Seasonal Climate
Variability and Implications for Seasonal Prediction. *Bulletin of the American Meteorological
Society*, 81(2), 255-264. [https://doi.org/10.1175/1520-0477\(2000\)081<0255:AOACMO>2.3.CO;2](https://doi.org/10.1175/1520-0477(2000)081<0255:AOACMO>2.3.CO;2)

Latif, M., & Barnett, T. P. (1994). Causes of Decadal Climate Variability over the North
Pacific and North America. *Science*, 266(5185), 634-637.
<https://doi.org/10.1126/science.266.5185.634>

Lau, N.-C. (1981). A Diagnostic Study of Recurrent Meteorological Anomalies Appearing in a 15-Year Simulation with a GFDL General Circulation Model. *Monthly Weather Review*, 109(11), 2287-2311. [https://doi.org/10.1175/1520-0493\(1981\)109<2287:ADSORM>2.0.CO;2](https://doi.org/10.1175/1520-0493(1981)109<2287:ADSORM>2.0.CO;2)

Leathers, D. J., Yarnal, B., & Palecki, M. A. (1991). The Pacific/North American Teleconnection Pattern and United States Climate. Part I: Regional Temperature and Precipitation Associations. *Journal of Climate*, 4(5), 517-528. [https://doi.org/10.1175/1520-0442\(1991\)004<0517:TPATPA>2.0.CO;2](https://doi.org/10.1175/1520-0442(1991)004<0517:TPATPA>2.0.CO;2)

Levene, H. (1960). Robust tests for equality of variances. In *Contributions to Probability and Statistics* (Vol. 1, pp. 278–292). Stanford University Press, Palo Alto.

Li, T., Zhang, Y., Lu, E., & Wang, D. (2002). Relative role of dynamic and thermodynamic processes in the development of the Indian Ocean dipole: An OGCM diagnosis. *Geophysical Research Letters*, 29(23), 25-21-25-24. <https://doi.org/10.1029/2002GL015789>

Lin, H., & Derome, J. (1999). The genesis and predictability of persistent Pacific–North American anomalies in a model atmosphere. *Tellus A: Dynamic Meteorology and Oceanography*. <https://doi.org/10.3402/tellusa.v51i5.14487>

Lorenz, E. N. (1963). Deterministic Nonperiodic Flow. *Journal of Atmospheric Sciences*, 20(2), 130-141. [https://doi.org/10.1175/1520-0469\(1963\)020<0130:DNF>2.0.CO;2](https://doi.org/10.1175/1520-0469(1963)020<0130:DNF>2.0.CO;2)

Lorenz, E. N. (1969). The predictability of a flow which possesses many scales of motion. *Tellus A: Dynamic Meteorology and Oceanography*. <https://doi.org/10.3402/tellusa.v21i3.10086>

Luo, J.-J., Masson, S., Behera, S. K., & Yamagata, T. (2008). Extended ENSO Predictions Using a Fully Coupled Ocean–Atmosphere Model. *Journal of Climate*, 21(1), 84-93. <https://doi.org/https://doi.org/10.1175/2007JCLI1412.1>

Luo, J. J., Masson, S., Behera, S., Delecluse, P., Gualdi, S., Navarra, A., & Yamagata, T. (2003). South Pacific origin of the decadal ENSO-like variation as simulated by a coupled GCM. *Geophysical Research Letters*, 30. <https://doi.org/10.1029/2003GL018649>

Luo, J. J., Masson, S., Behera, S., Shingu, S., & Yamagata, T. (2005). Seasonal Climate Predictability in a Coupled OAGCM Using a Different Approach for Ensemble Forecasts. *Journal of Climate*, 18(21), 4474-4497. <https://doi.org/10.1175/JCLI3526.1>

Luo, J. J., Masson, S., Roeckner, E., Madec, G., & Yamagata, T. (2005). Reducing climatology bias in an ocean–atmosphere CGCM with improved coupling physics. *Journal of Climate*, 18, 2344-2360. <https://doi.org/10.1175/JCLI3404.1>

Madec, G., Delecluse, P., Imbard, M., & Lévy, C. (1998). *OPA 8.1 Ocean General Circulation Model reference manual* [Software]. LODYC/IPSL Tech. Rep. Note 11. https://www.researchgate.net/publication/243055542_OPA_81_Ocean_General_Circulation_Model_reference_manual

Madec, G., & Imbard, M. (1996). A global ocean mesh to overcome the North Pole singularity. *Climate Dynamics*, 12(6), 381-388. <https://doi.org/10.1007/BF00211684>

Matsuno, T. (1966). Quasi-Geostrophic Motions in the Equatorial Area. *Journal of the Meteorological Society of Japan. Ser. II*, 44(1), 25-43. https://doi.org/10.2151/jmsj1965.44.1_25

Mitchell, D. M., Thorne, P. W., Stott, P. A., & Gray, L. J. (2013). Revisiting the controversial issue of tropical tropospheric temperature trends. *Geophysical Research Letters*, 40(11), 2801-2806. <https://doi.org/10.1002/grl.50465>

Moon, H., & Ha, K.-J. (2020). Distinguishing changes in the Hadley circulation edge. *Theoretical and Applied Climatology*, 139(3), 1007-1017. <https://doi.org/10.1007/s00704-019-03017-1>

Neelin, J. D., Latif, M., & Jin, F. (1994). Dynamics of Coupled Ocean-Atmosphere Models: The Tropical Problem. *Annual Review of Fluid Mechanics*, 26(1), 617-659. <https://doi.org/10.1146/annurev.fl.26.010194.003153>

Ng, B., Cai, W., Cowan, T., & Bi, D. (2018). Influence of internal climate variability on Indian Ocean Dipole properties. *Scientific Reports*, 8(1), 13500. <https://doi.org/10.1038/s41598-018-31842-3>

Pacanowski, R. C. (1987). Effect of Equatorial Currents on Surface Stress. *Journal of Physical Oceanography*, 17(6), 833-838. [https://doi.org/10.1175/1520-0485\(1987\)017<0833:EOECOS>2.0.CO;2](https://doi.org/10.1175/1520-0485(1987)017<0833:EOECOS>2.0.CO;2)

Qiu, B., & Chen, S. (2010). Eddy-mean flow interaction in the decadal modulating Kuroshio Extension system. *Deep Sea Research Part II: Topical Studies in Oceanography*, 57(13), 1098-1110. <https://doi.org/10.1016/j.dsr2.2008.11.036>

Qiu, B., & Kelly, K. A. (1993). Upper-Ocean Heat Balance in the Kuroshio Extension Region. *Journal of Physical Oceanography*, 23(9), 2027-2041. [https://doi.org/10.1175/1520-0485\(1993\)023<2027:UOHBIT>2.0.CO;2](https://doi.org/10.1175/1520-0485(1993)023<2027:UOHBIT>2.0.CO;2)

801 Rieger, N., & Levang, S. J. (2024). xeofs: Comprehensive EOF analysis in Python with
802 xarray [software]. *Journal of Open Source Software*, 9, 6060, Article 93.
803 <https://doi.org/10.21105/joss.06060>

804 Rind, D. (1999). Complexity and Climate. *Science*, 284(5411), 105-107.
805 <https://doi.org/10.1126/science.284.5411.105>

806 Rodionov, S., & Assel, R. (2001). A new look at the Pacific/North American Index.
807 *Geophysical Research Letters*, 28(8), 1519-1522. <https://doi.org/10.1029/2000GL012185>

808 Roeckner, E., Arpe, K., Bengtsson, L., Christoph, M., Claussen, M., Duemenil, L., . . .
809 Schulzweida, U. (1996). *The atmospheric general circulation model ECHAM-4: Model*
810 *description and simulation of present-day climate* [Software]. [https://hdl.handle.net/11858/00-](https://hdl.handle.net/11858/00-001M-0000-0013-ADE3-C)
811 [001M-0000-0013-ADE3-C](https://hdl.handle.net/11858/00-001M-0000-0013-ADE3-C)

812 Saji, N. H., Goswami, B. N., Vinayachandran, P. N., & Yamagata, T. (1999). A dipole
813 mode in the tropical Indian Ocean. *Nature*, 401(6751), 360-363. <https://doi.org/10.1038/43854>

814 Schulz, M., & Mudelsee, M. (2002). REDFIT: estimating red-noise spectra directly from
815 unevenly spaced paleoclimatic time series [Software]. *Computers & Geosciences*, 28(3), 421-426.
816 [https://doi.org/10.1016/S0098-3004\(01\)00044-9](https://doi.org/10.1016/S0098-3004(01)00044-9)

817 Selten, F. M., Duane, G. S., Wiegerinck, W., Keenlyside, N., Kurths, J., & Kocarev, L.
818 (2011). Supermodeling by Combining Imperfect Models. *Procedia Computer Science*, 7, 261-263.
819 <https://doi.org/https://doi.org/10.1016/j.procs.2011.09.025>

Shapiro, S. S., & Wilk, M. B. (1965). An analysis of variance test for normality (complete samples)[†]. *Biometrika*, 52(3-4), 591-611. <https://doi.org/10.1093/biomet/52.3-4.591>

Shen, M.-L., Keenlyside, N., Selten, F., Wiegerinck, W., & Duane, G. S. (2016). Dynamically combining climate models to “supermodel” the tropical Pacific. *Geophysical Research Letters*, 43(1), 359-366. <https://doi.org/10.1002/2015GL066562>

Shenyulu. (2024). *shenyulu/easyclimate*. In (Version 2024.01.01) [Software]. Zenodo. <https://doi.org/10.5281/zenodo.10457357>

Shukla, J. (1981). Dynamical Predictability of Monthly Means. *Journal of Atmospheric Sciences*, 38(12), 2547-2572. [https://doi.org/10.1175/1520-0469\(1981\)038<2547:DPOMM>2.0.CO;2](https://doi.org/10.1175/1520-0469(1981)038<2547:DPOMM>2.0.CO;2)

Shukla, J., Anderson, J., Baumhefner, D., Brankovic, C., Chang, Y., Kalnay, E., . . . Tribbia, J. (2000). Dynamical Seasonal Prediction. *Bulletin of the American Meteorological Society*, 81(11), 2593-2606. [https://doi.org/10.1175/1520-0477\(2000\)081<2593:DSP>2.3.CO;2](https://doi.org/10.1175/1520-0477(2000)081<2593:DSP>2.3.CO;2)

Straus, D., Shukla, J., Paolino, D., Schubert, S., Suarez, M., Pegion, P., & Kumar, A. (2003). Predictability of the Seasonal Mean Atmospheric Circulation during Autumn, Winter, and Spring. *Journal of Climate*, 16(22), 3629-3649. [https://doi.org/10.1175/1520-0442\(2003\)016<3629:POTSMA>2.0.CO;2](https://doi.org/10.1175/1520-0442(2003)016<3629:POTSMA>2.0.CO;2)

Straus, D. M., & Shukla, J. (2000). Distinguishing between the SST-forced variability and internal variability in mid latitudes: Analysis of observations and GCM simulations. *Quarterly*

840 *Journal of the Royal Meteorological Society*, 126(567), 2323-2350.
841 <https://doi.org/10.1002/qj.49712656716>

842 Stuecker, M. F. (2018). Revisiting the Pacific Meridional Mode. *Scientific Reports*, 8(1),
843 3216. <https://doi.org/10.1038/s41598-018-21537-0>

844 Valcke, S., Terray, L., & Piacentini, A. (2000). OASIS 2.4 Ocean Atmosphere Soil User's
845 Guide [Software].
846 [https://www.researchgate.net/publication/2801458_OASIS_24_Ocean_Atmosphere_Soil_User%](https://www.researchgate.net/publication/2801458_OASIS_24_Ocean_Atmosphere_Soil_User%27s_Guide)
847 [27s_Guide](https://www.researchgate.net/publication/2801458_OASIS_24_Ocean_Atmosphere_Soil_User%27s_Guide)

848 van den Berge, L. A., Selten, F. M., Wiegerinck, W., & Duane, G. S. (2011). A multi-
849 model ensemble method that combines imperfect models through learning. *Earth Syst. Dynam.*,
850 2(1), 161-177. <https://doi.org/10.5194/esd-2-161-2011>

851 Van den Dool, H. M., Peng, P., Johansson, Å., Chelliah, M., Shabbar, A., & Saha, S.
852 (2006). Seasonal-to-Decadal Predictability and Prediction of North American Climate—The
853 Atlantic Influence. *Journal of Climate*, 19(23), 6005-6024. <https://doi.org/10.1175/JCLI3942.1>

854 Virtanen, P., Gommers, R., Oliphant, T. E., Haberland, M., Reddy, T., Cournapeau, D., . .
855 . SciPy, C. (2020). SciPy 1.0: fundamental algorithms for scientific computing in Python
856 [Software]. *Nature Methods*, 17(3), 261-272. <https://doi.org/10.1038/s41592-019-0686-2>

857 Wallace, J. M., & Gutzler, D. S. (1981). Teleconnections in the Geopotential Height Field
858 during the Northern Hemisphere Winter. *Monthly Weather Review*, 109(4), 784-812.
859 [https://doi.org/10.1175/1520-0493\(1981\)109<0784:TITGHF>2.0.CO;2](https://doi.org/10.1175/1520-0493(1981)109<0784:TITGHF>2.0.CO;2)

White, G. H. (1980). Skewness, Kurtosis and Extreme Values of Northern Hemisphere Geopotential Heights. *Monthly Weather Review*, 108(9), 1446-1455. [https://doi.org/10.1175/1520-0493\(1980\)108<1446:SKAEVO>2.0.CO;2](https://doi.org/10.1175/1520-0493(1980)108<1446:SKAEVO>2.0.CO;2)

Wu, R., & Kirtman, B. P. (2003). On the impacts of the Indian summer monsoon on ENSO in a coupled GCM. *Quarterly Journal of the Royal Meteorological Society*, 129(595), 3439-3468. <https://doi.org/10.1256/qj.02.214>

Wu, R., & Kirtman, B. P. (2005). Roles of Indian and Pacific Ocean air-sea coupling in tropical atmospheric variability. *Climate Dynamics*, 25(2), 155-170. <https://doi.org/10.1007/s00382-005-0003-x>

Wu, R., & Kirtman, B. P. (2006). Changes in Spread and Predictability Associated with ENSO in an Ensemble Coupled GCM. *Journal of Climate*, 19(17), 4378-4396. <https://doi.org/10.1175/JCLI3872.1>

Xin, X., Xue, W., Zhang, M., Li, H., Zhang, T., & Zhang, J. (2014). Simulation of SST variability in the North Pacific Ocean and ENSO by an interactive ensemble coupled model. *Chinese Journal of Geophysics (in Chinese)*, 57(4), 1021-1031. <https://doi.org/10.6038/cjg20140401>

Yeh, S.-W., & Kirtman, B. P. (2006). The characteristics of signal versus noise sst variability in the north pacific and the tropical pacific ocean. *Ocean Science Journal*, 41(1), 1-10. <https://doi.org/10.1007/BF03022401>

879 Yeh, S.-W., & Kirtman, B. P. (2009). Internal Atmospheric Variability and Interannual-to-
880 Decadal ENSO Variability in a CGCM. *Journal of Climate*, 22(9), 2335-2355.
881 <https://doi.org/10.1175/2008JCLI2240.1>

882 Yeh, S.-W., Kirtman, B. P., & An, S.-I. (2007). Local versus non-local atmospheric
883 weather noise and the North Pacific SST variability. *Geophysical Research Letters*, 34(14).
884 <https://doi.org/10.1029/2007GL030206>

885 Yeh, S. W., & Kirtman, B. P. (2004). The impact of internal atmospheric variability on the
886 North Pacific SST variability. *Climate Dynamics*, 22(6), 721-732. [https://doi.org/10.1007/s00382-](https://doi.org/10.1007/s00382-004-0399-8)
887 004-0399-8

888 Zhang, J., Xue, W., Zhang, M., Li, H., Zhang, T., Li, L., & Xin, X. (2014). Climate impacts
889 of stochastic atmospheric perturbations on the ocean. *International Journal of Climatology*,
890 34(15), 3900-3912. <https://doi.org/10.1002/joc.3949>

891 Zhang, Y. (2024a). *Hydra-SINTEX datasets* [datasets].
892 <https://doi.org/10.6084/m9.figshare.24978648.v3>

893 Zhang, Y. (2024b). *SINTEX-F datasets* [datasets].
894 <https://doi.org/10.6084/m9.figshare.24978633.v2>

895 Zhao, J., Sung, M.-K., Park, J.-H., Luo, J.-J., & Kug, J.-S. (2023). Part I observational
896 study on a new mechanism for North Pacific Oscillation influencing the tropics. *npj Climate and*
897 *Atmospheric Science*, 6(1), 15. <https://doi.org/10.1038/s41612-023-00336-z>

898 Zwiers, F. W. (1996). Interannual variability and predictability in an ensemble of AMIP
899 climate simulations conducted with the CCC GCM2. *Climate Dynamics*, 12(12), 825-847.
900 <https://doi.org/10.1007/s003820050146>

Figure 1.

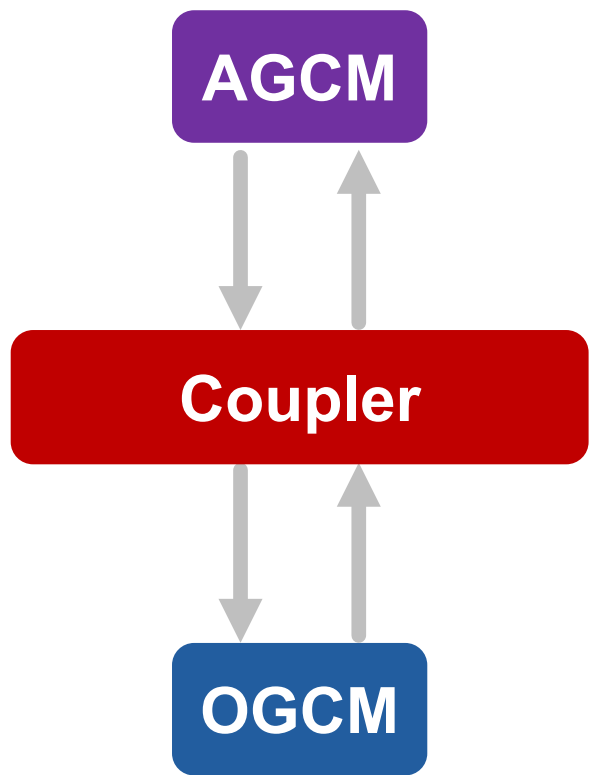
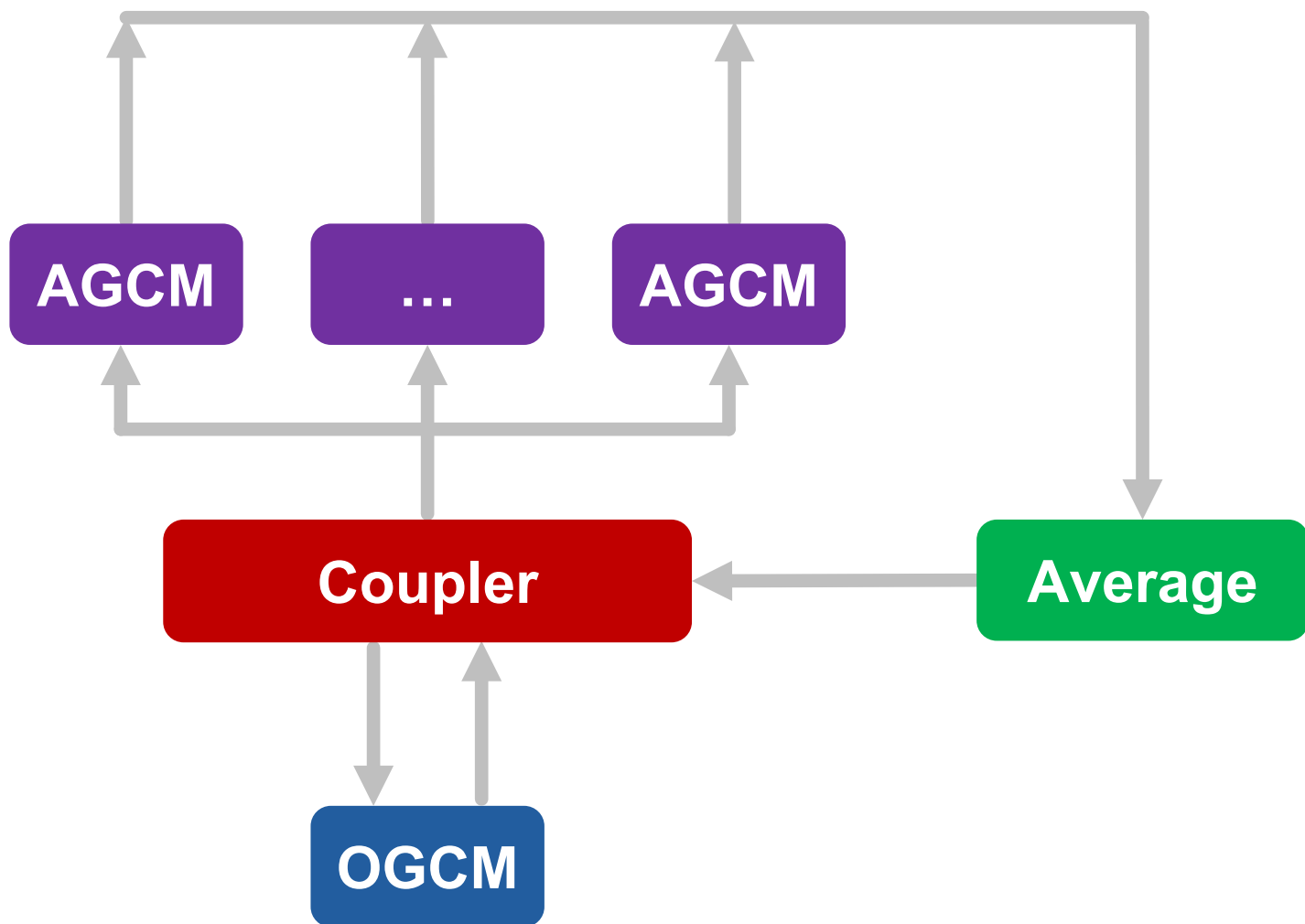
a**SINTEX-F****b****Hydra-SINTEX**

Figure 2.

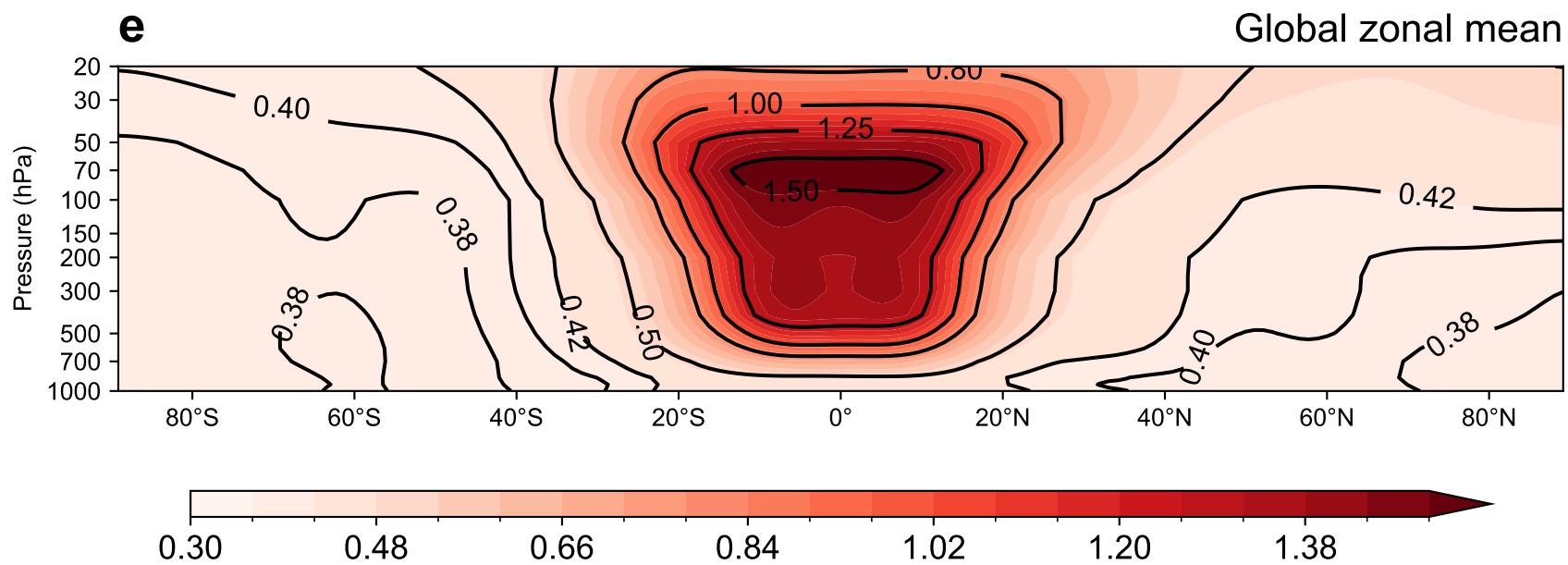
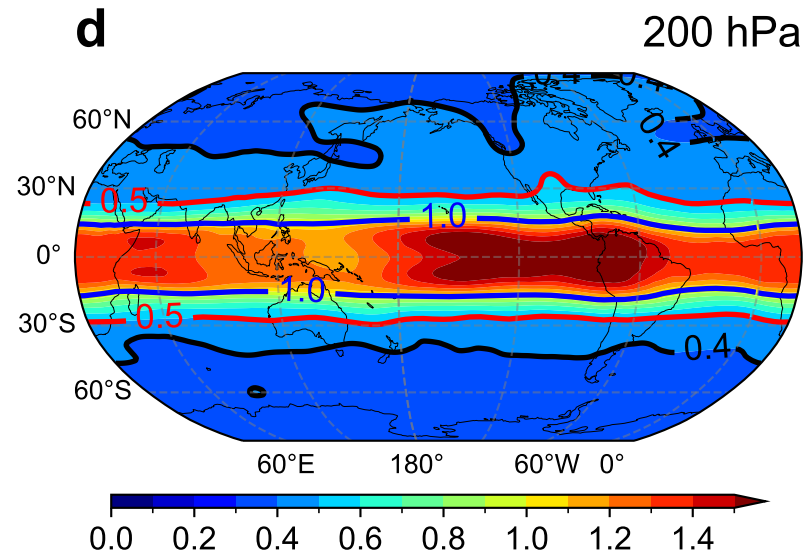
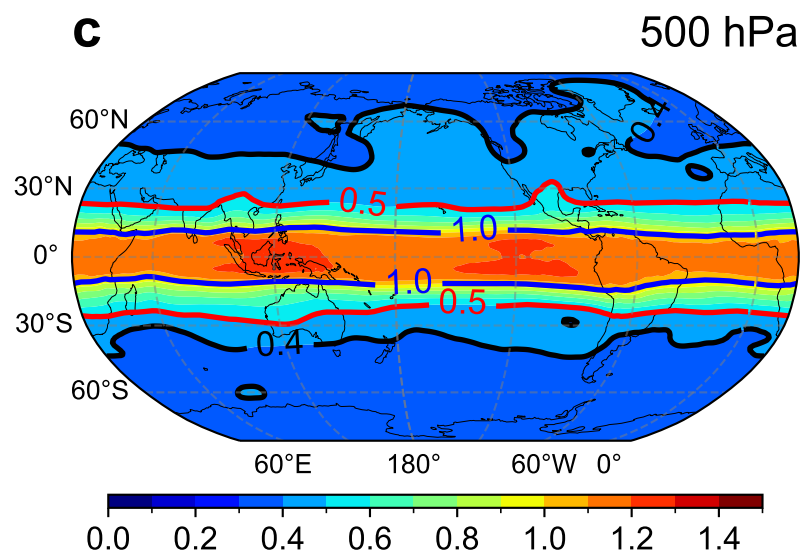
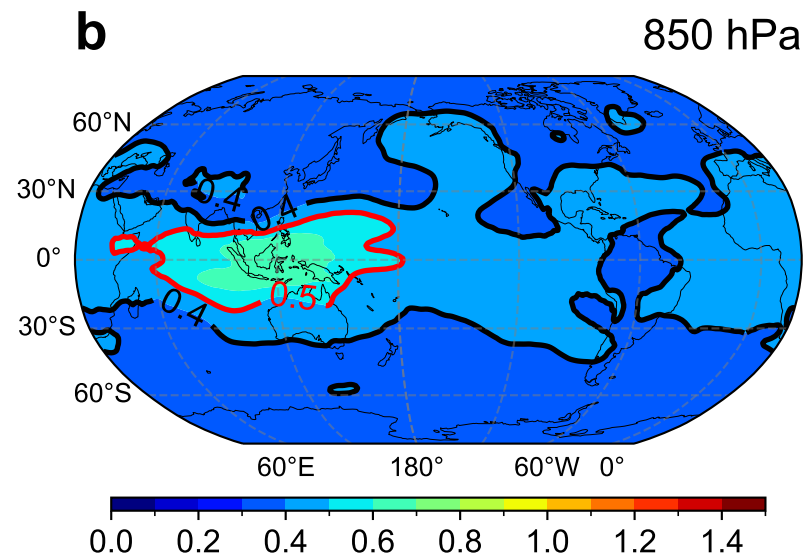
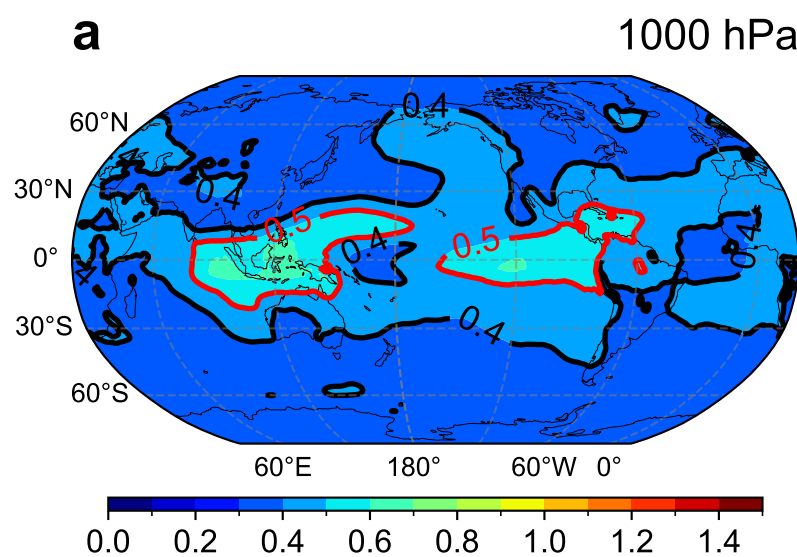
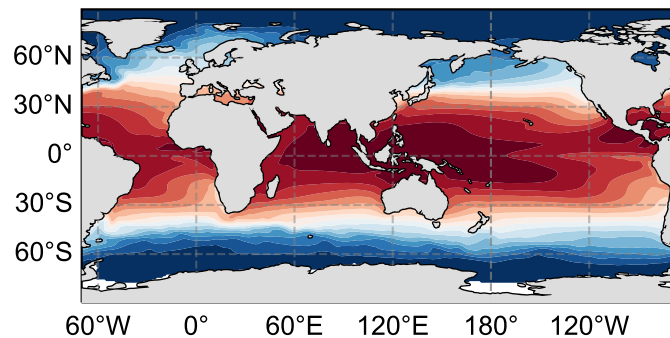
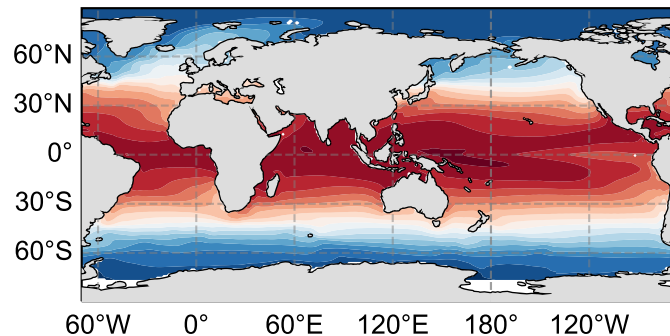


Figure 3.

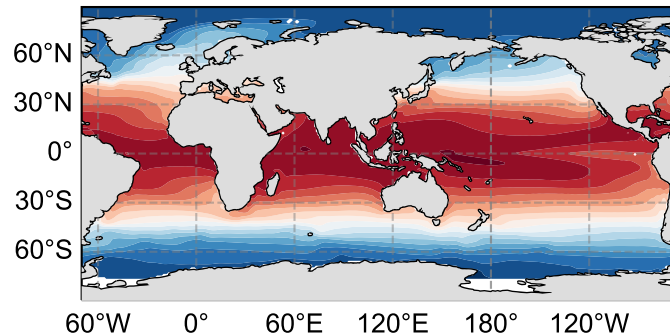
a Obs



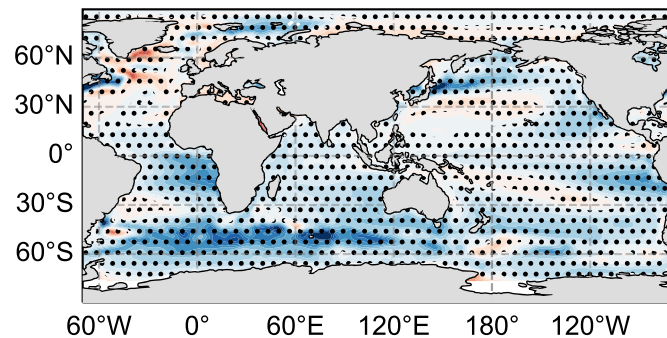
b SINTEX-F



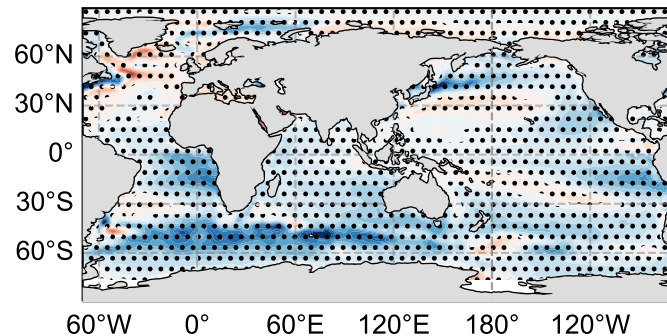
c Hydra-SINTEX



d Obs - SINTEX-F



e Obs - Hydra-SINTEX



f AIV effects
(SINTEX-F - Hydra-SINTEX)

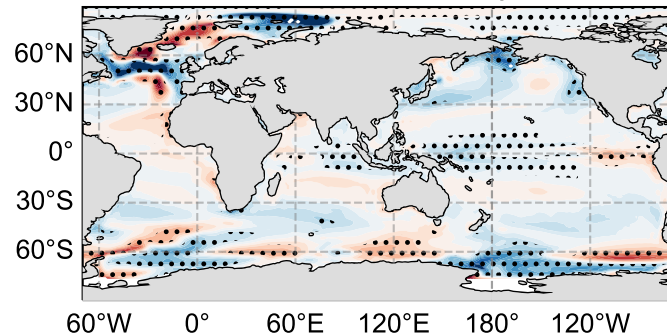


Figure 4.

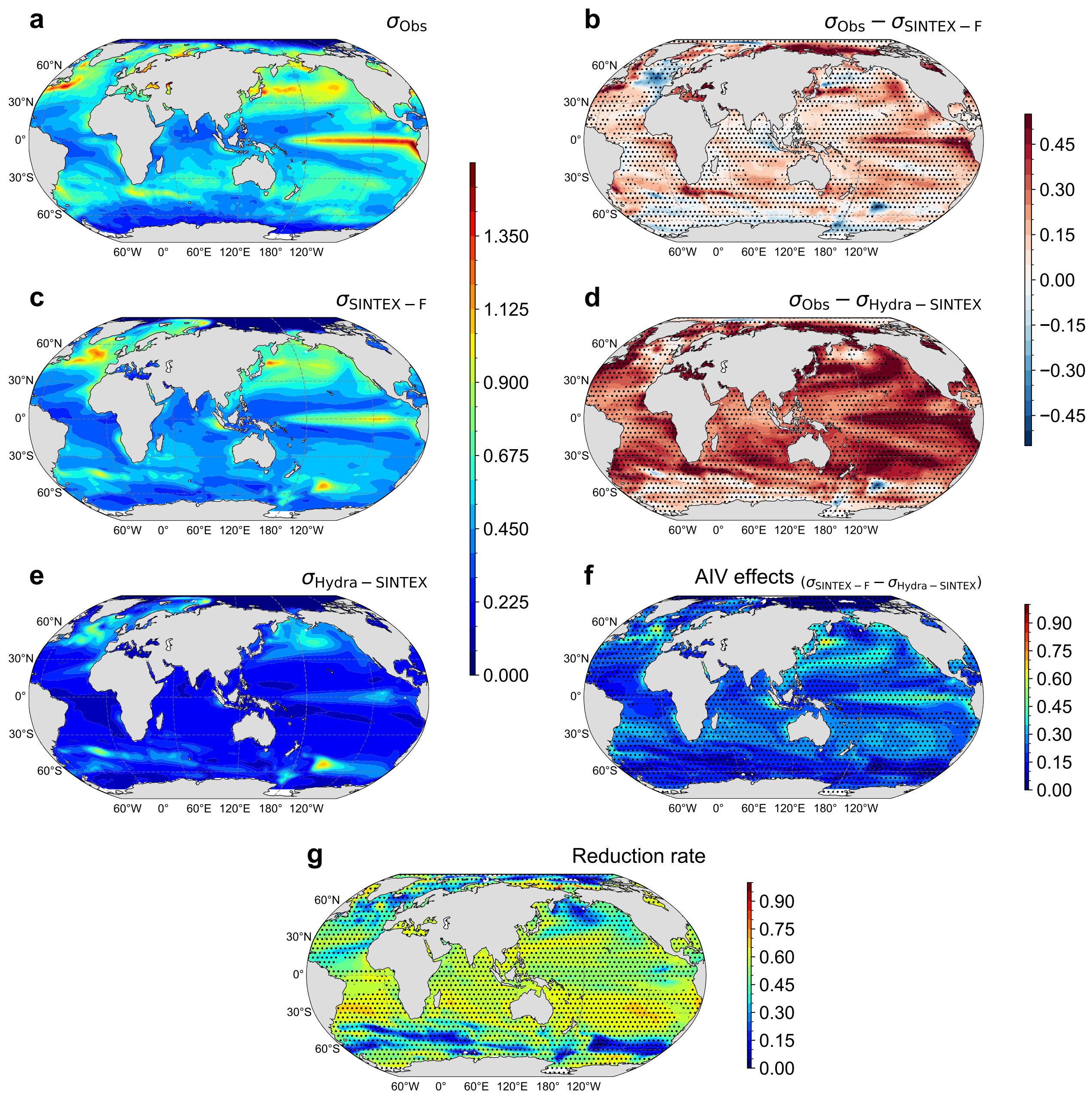


Figure 5.

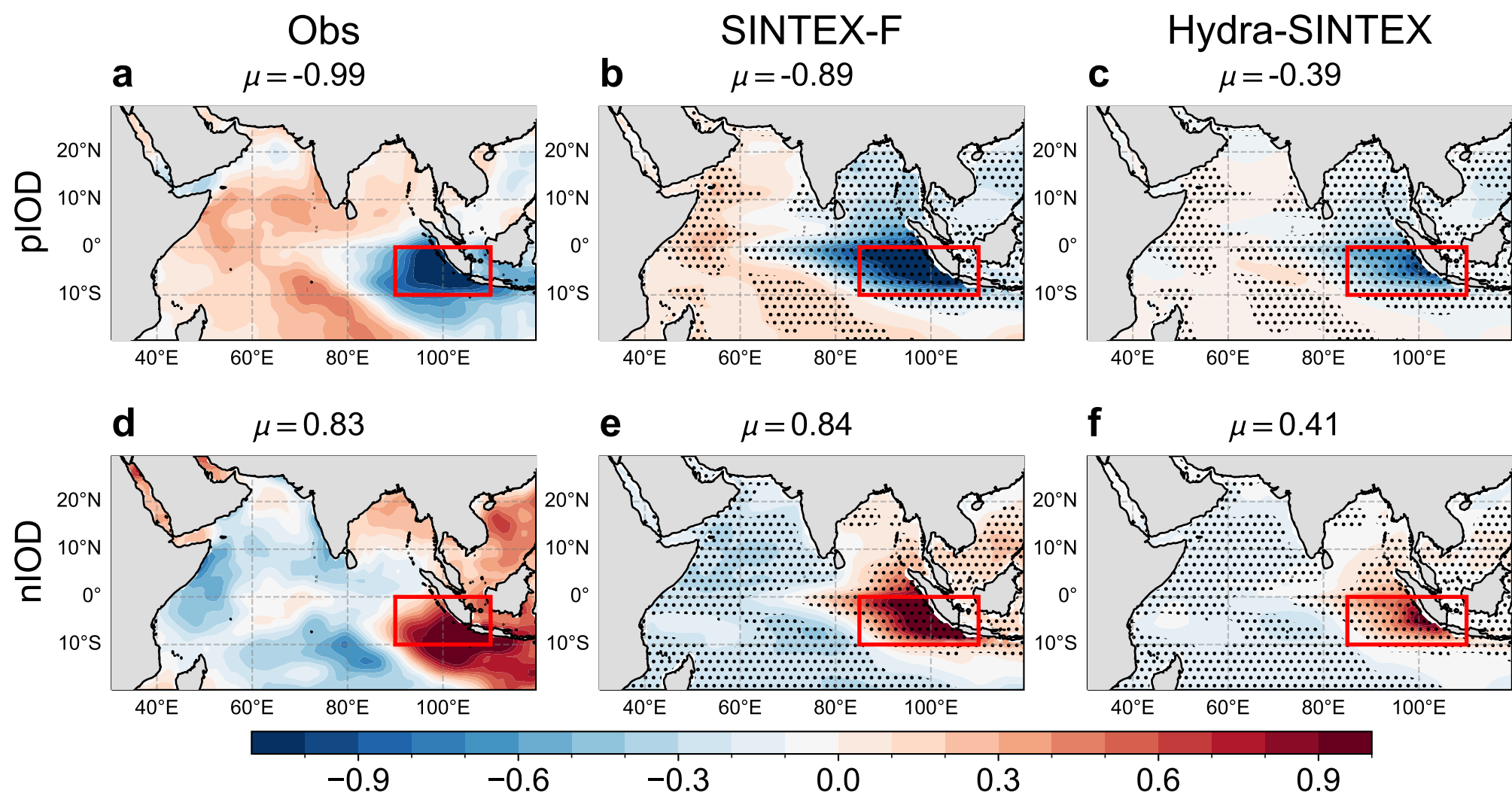


Figure 6.

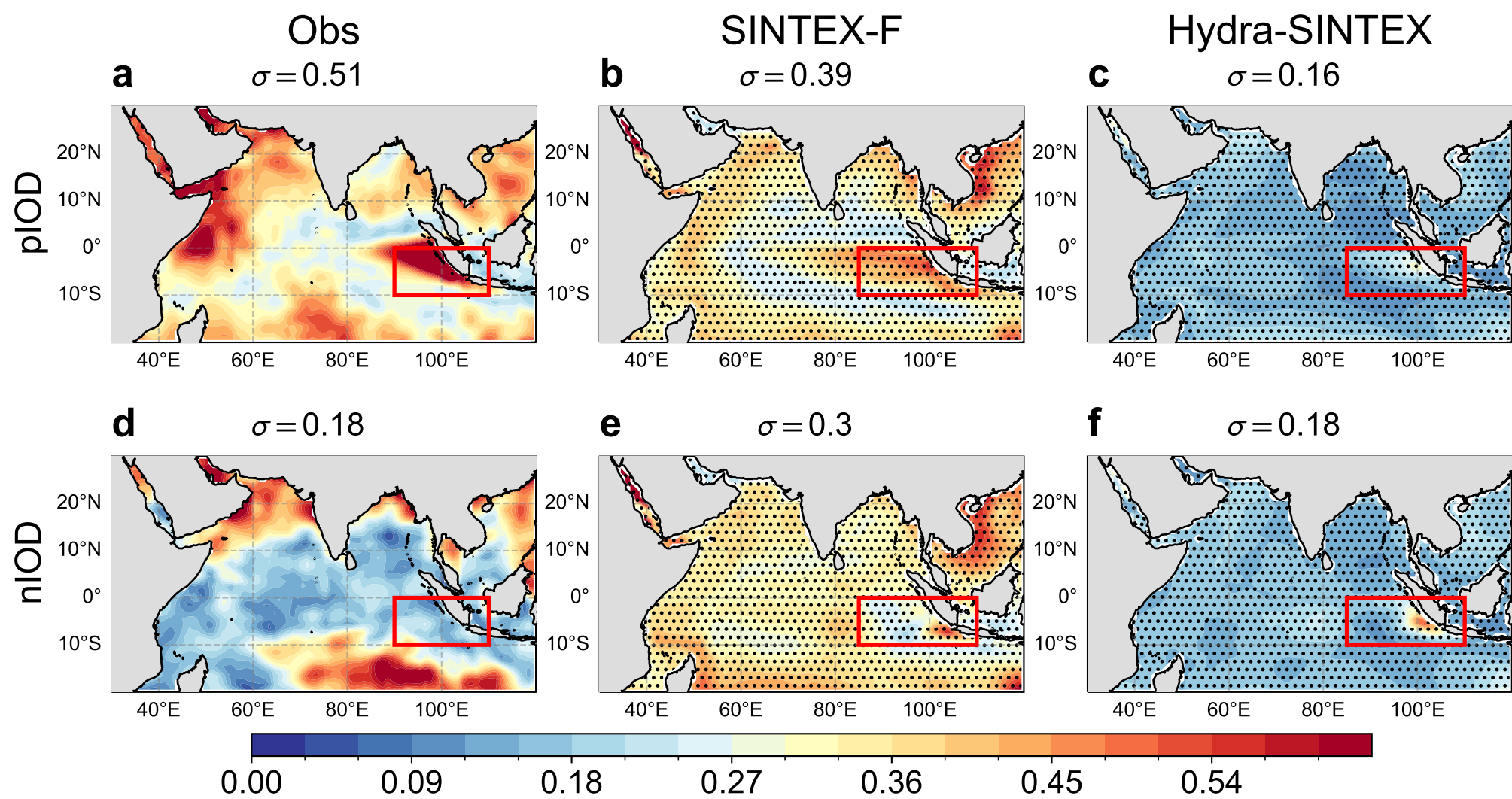
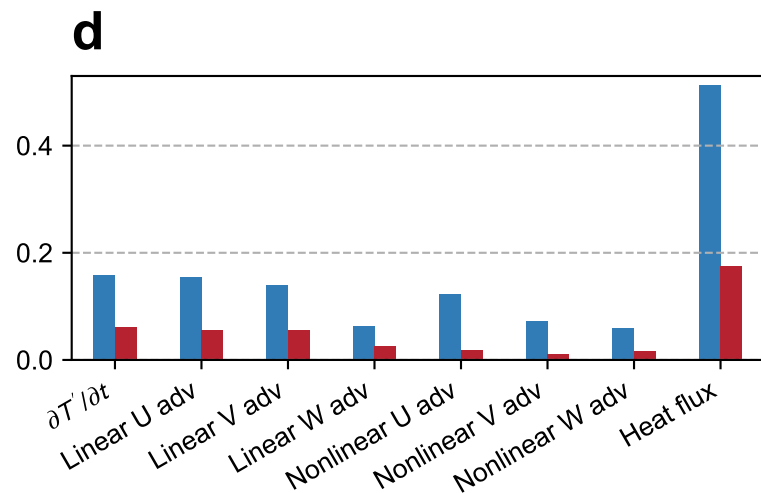
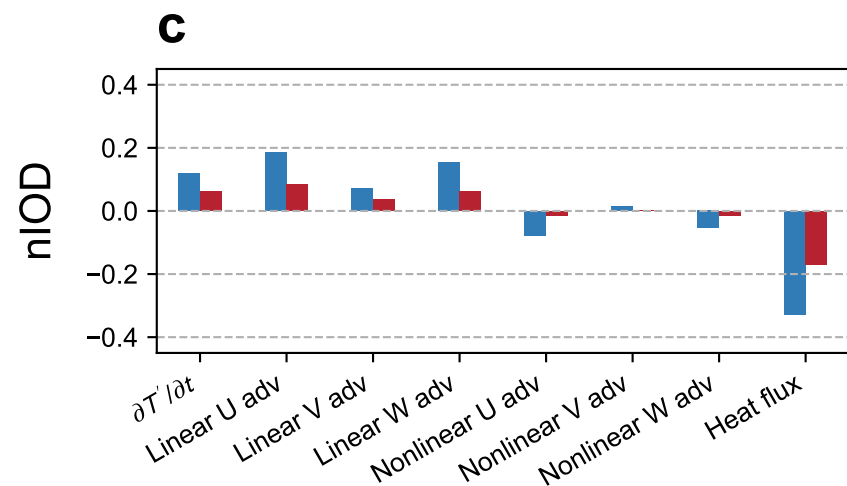
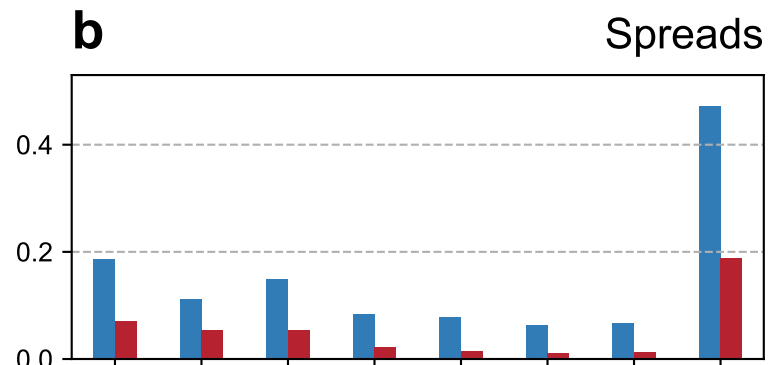
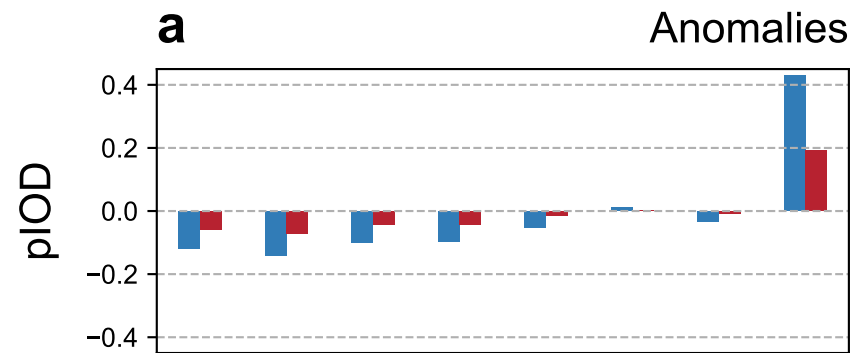


Figure 7.



SINTEX-F Hydra-SINTEX

Figure 8.

SINTEX-F

Hydra-SINTEX

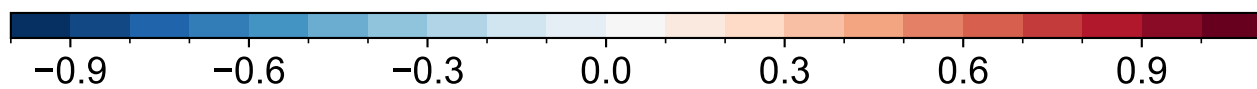
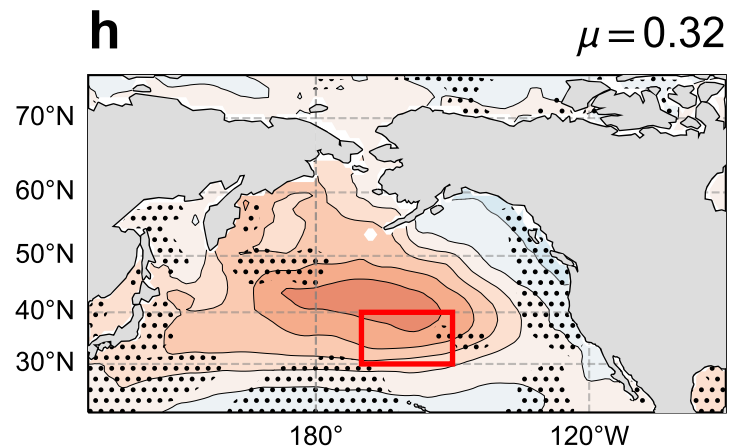
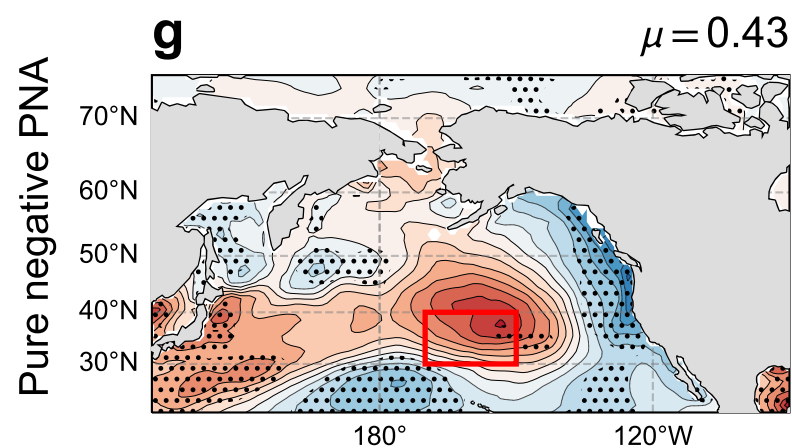
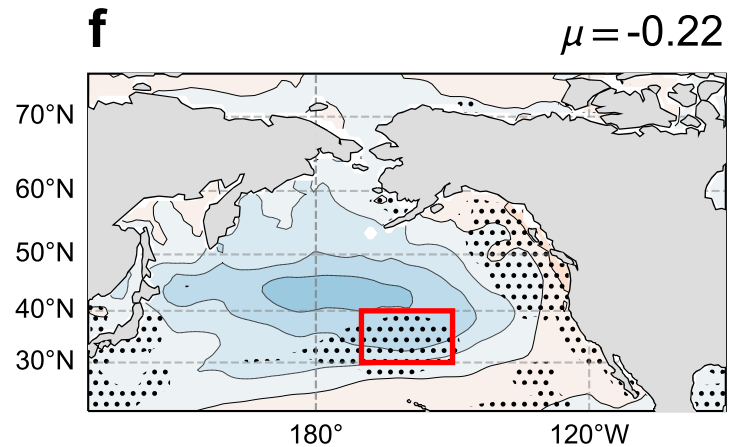
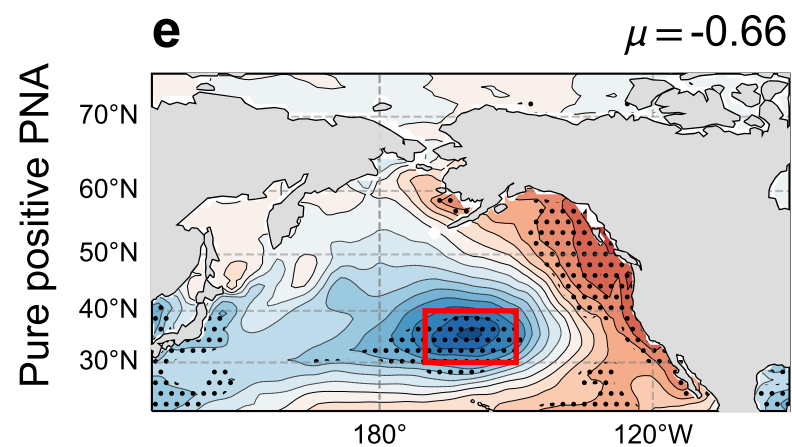
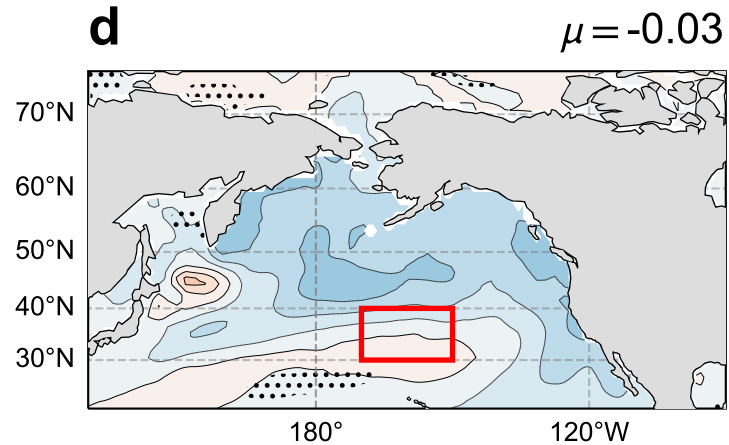
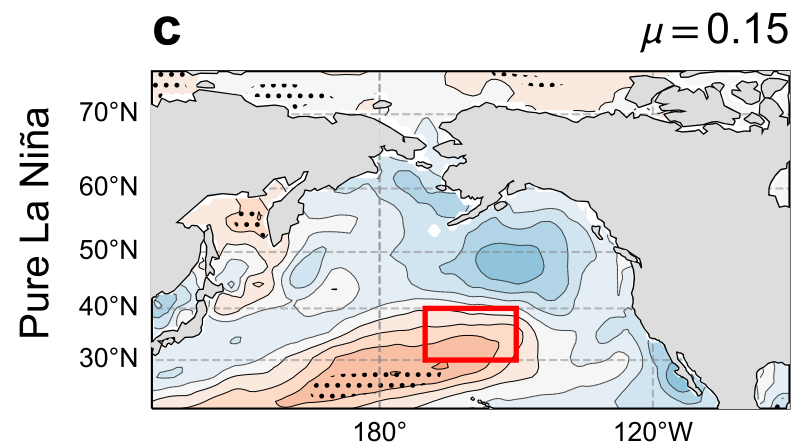
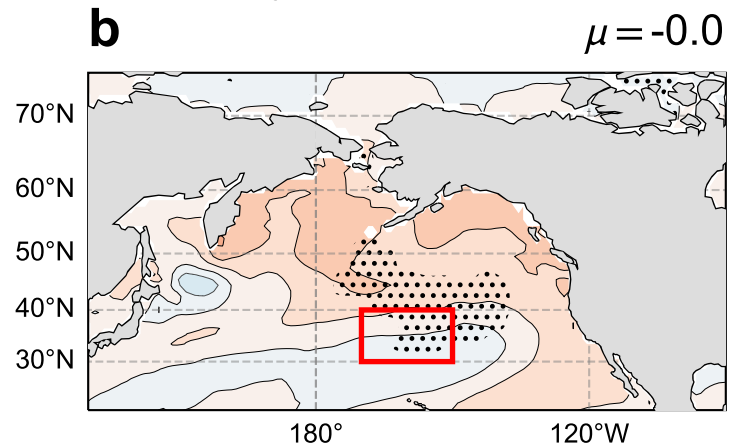
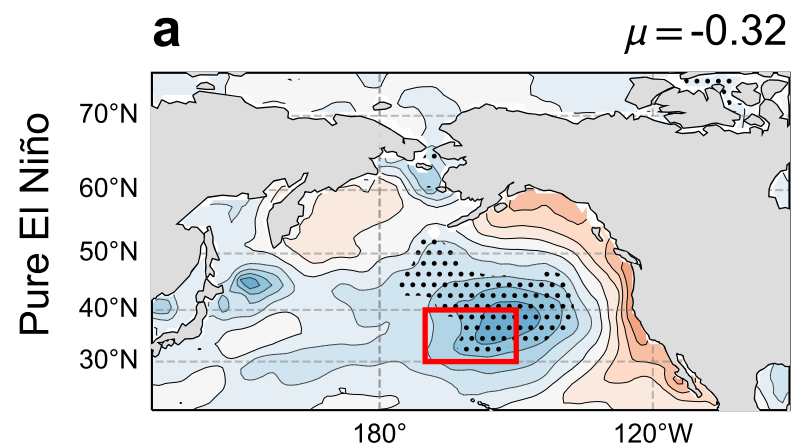


Figure 9.

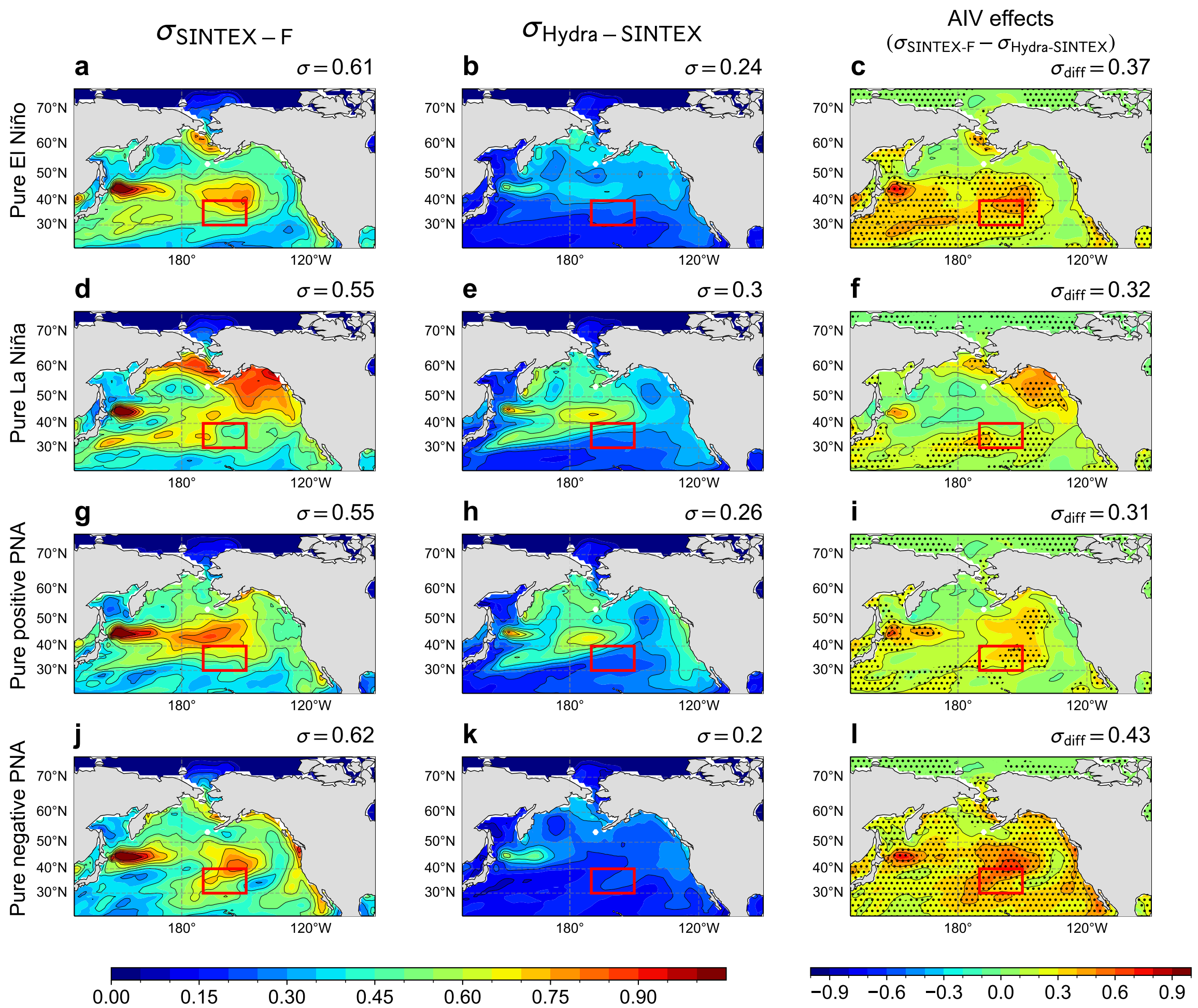


Figure 10.

